



AFRL-OSR-VA-TR-2013-0215

ON THE FLOW PHYSICS OF EFFECTIVELY CONTROLLED OPEN CAVITY FLOWS

Lawrence Ukeiley and Louis Cattafesta
University of Florida

May 2013
Final Report

DISTRIBUTION A: Approved for public release.

AIR FORCE RESEARCH LABORATORY
AF OFFICE OF SCIENTIFIC RESEARCH (AFOSR)
ARLINGTON, VIRGINIA 22203
AIR FORCE MATERIEL COMMAND

REPORT DOCUMENTATION PAGE				Form Approved OMB No. 0704-0188	
<small>The public reporting burden for this collection of information is estimated to average 1 hour per response, including the time for reviewing instructions, searching existing data sources, gathering and maintaining the data needed, and completing and reviewing the collection of information. Send comments regarding this burden estimate or any other aspect of this collection of information, including suggestions for reducing the burden, to the Department of Defense, Executive Services and Communications Directorate (0704-0188). Respondents should be aware that notwithstanding any other provision of law, no person shall be subject to any penalty for failing to comply with a collection of information if it does not display a currently valid OMB control number.</small>					
PLEASE DO NOT RETURN YOUR FORM TO THE ABOVE ORGANIZATION.					
1. REPORT DATE (DD-MM-YYYY) 19-10-2012		2. REPORT TYPE FINAL REPORT		3. DATES COVERED (From - To) 8/1/2009-7/31/2012	
4. TITLE AND SUBTITLE ON THE FLOW PHYSICS OF EFFECTIVELY CONTROLLED OPEN CAVITY FLOWS				5a. CONTRACT NUMBER	
				5b. GRANT NUMBER FA9550-09-1-0573	
				5c. PROGRAM ELEMENT NUMBER	
6. AUTHOR(S) Lawrence Ukeiley and Louis Cattafesta				5d. PROJECT NUMBER	
				5e. TASK NUMBER	
				5f. WORK UNIT NUMBER	
7. PERFORMING ORGANIZATION NAME(S) AND ADDRESS(ES) University of Florida, Office of Engineering Research 339 Weil Hall /PO BOX 116550 Gainesville, FL 32611-6550				8. PERFORMING ORGANIZATION REPORT NUMBER	
9. SPONSORING/MONITORING AGENCY NAME(S) AND ADDRESS(ES) Air Force Office of Scientific Research 875 North Randolph Street, Suite 326 Arlington VA 22203-1768				10. SPONSOR/MONITOR'S ACRONYM(S) AFOSR	
				11. SPONSOR/MONITOR'S REPORT NUMBER(S) AFRL-OSR-VA-TR-2013-0215	
12. DISTRIBUTION/AVAILABILITY STATEMENT DISTRIBUTION A: APPROVED FOR PUBLIC RELEASE					
13. SUPPLEMENTARY NOTES Cavity Flow, Flow Control					
14. ABSTRACT The intense aeroacoustic environment of flow over open cavities is created by an important fundamental flow phenomena associated with a resonating fluid system. In practical applications, this resonating flow can be extremely detrimental to aircraft due to the creation of high levels of broadband and tonal fluctuating pressures. The ability to alter flow field characteristics for a practical advantage represents a significant challenge that, when accomplished, can lead to paradigm shift in how systems involving fluid flow are designed. The research reported in this document represents accomplishments on controlling the flow over open cavities and developing a better understanding on how leading edge actuation alters the flow. The two focuses of this research, detailed flow measurements of successful active control strategies and development of adaptive control strategies, have both advanced the knowledge active as applied to high speed flow over open cavities. On the flow measurement side, we have explored the evolution of flow downstream of segmented leading edge blowing slots.					
15. SUBJECT TERMS Cavity Flow, Flow Control					
16. SECURITY CLASSIFICATION OF:			17. LIMITATION OF ABSTRACT SAR	18. NUMBER OF PAGES 49	19a. NAME OF RESPONSIBLE PERSON
a. REPORT U	b. ABSTRACT U	c. THIS PAGE U			19b. TELEPHONE NUMBER (Include area code)

Reset

**ON THE FLOW PHYSICS OF EFFECTIVELY CONTROLLED OPEN CAVITY
FLOWS**

FINAL REPORT
AFOSR GRANT FA9550-09-1-0573

By

Lawrence Ukeiley and Louis Cattafesta

Department of Mechanical and Aerospace Engineering
University of Florida

Abstract	3
1 Introduction.....	4
1.1 Motivation.....	4
1.2 Background.....	4
1.2.1 Control of Cavity Flows	5
1.3 Objectives	6
1.4 Layout of this Document	7
2 Steady Blowing.....	8
2.1 Supersonic Application.....	8
2.1.1 Facility and Experimental Setup.....	8
2.1.2 Results	11
2.1.3 Summary.....	22
2.2 Subsonic Application.....	23
2.2.1 Facility and Experimental Setup.....	23
2.2.2 Results	25
2.2.3 Summary.....	29
3 Adaptive Control using Time Dependent Leading Edge Excitation	30
3.1 Control Algorithms	30
3.1.1 Downhill Simplex Algorithm	30
3.1.2 ARMARKOV Adaptive Disturbance Rejection Algorithm	31
3.1.3 Generalized Predictive Control Algorithm.....	33
3.2 Actuators	34
3.3 Actuator Characterization	36
3.4 Flow Control Results	38
3.5 Summary	43
4 Project Summary and Future Work	44
5 Publications and Students Supported.....	45
5.1 Students/Post Docs.....	45
5.2 Publications/Presentations	45
6 List of References	47

Abstract

The intense aeroacoustic environment of flow over open cavities is created by an important fundamental flow phenomena associated with a resonating fluid system. In practical applications, this resonating flow can be extremely detrimental to aircraft due to the creation of high levels of broadband and tonal fluctuating pressures. The ability to alter flow field characteristics for a practical advantage represents a significant challenge that, when accomplished, can lead to paradigm shift in how systems involving fluid flow are designed. The research reported in this document represents accomplishments on controlling the flow over open cavities and developing a better understanding on how leading edge actuation alters the flow. The two focuses of this research, detailed flow measurements of successful active control strategies and development of adaptive control strategies, have both advanced the knowledge active as applied to high speed flow over open cavities. On the flow measurement side, we have explored the evolution of flow downstream of segmented leading edge blowing slots. These measurements have demonstrated how the streamwise evolution of streamwise aligned vortical structures can alter the location of where the cavity shear layer interacts with the aft wall, thus altering the source of the intense pressure fluctuation observed in high speed open cavity flows. On the adaptive control side, we have demonstrated the ability of common algorithms such as the Downhill Simplex method to perform better than open loop strategies with the same actuators and free stream flow conditions. The results in both phases of this study are encouraging in terms future endeavors to develop active control strategies in high speed flows.

1 Introduction

The primary goal of this research was to develop a better fundamental understanding of how flow control can be used to alter the flow over an open cavity with a long range goal of developing an adaptive control scheme effective in supersonic free stream conditions. To achieve this goal several advancements in our understanding of active control methodologies, as well as how flow actuation schemes fundamentally couple with the flow, are necessary. The work conducted as part of this effort has contributed to this understanding and demonstrated methodologies that can be used to achieve the ultimate goal of actively controlling open cavity flows. This first chapter introduces the flow physics of cavity flows by way of a brief discussion. Then, we will discuss some of the previous applications of control to cavity flows. This is followed by a brief statement of the objectives of the study which is in turn followed by section discussing the layout of the rest of this document.

1.1 Motivation

From the limited review that will be presented below, it is apparent that while progress has been made towards effective active suppression concepts, we do not yet understand the key physical mechanisms that need to be leveraged in the design of an effective control system without iteration. The current effort has demonstrated that active control strategies can be effective at controlling the flow at moderate subsonic Mach number and that the actuator configuration can significantly alter the effect of the actuation. However, in order to achieve the goal of using adaptive control at supersonic free stream Mach numbers, one needs to better understand the flow physics of the actuator flow coupling.

1.2 Background

Flow-induced cavity oscillation problems have attracted numerous researchers in both fluid dynamics and controls over the last few decades. These oscillations exist in many practical environments, such as sunroofs in automobiles as well as landing-gear and weapon bays on aircraft (Kook et al., 1997). The pressure fluctuations can exceed 170 dB (reference pressure of 20 μ Pa) and can potentially cause fatigue failure of the cavity structure and its contents. In addition, the cavity pressure fluctuations can increase drag (Rowley and Williams, 2006). These pressure fluctuations contain tonal and broad-band components, and both need to be suppressed for many practical applications.

The physical mechanisms responsible for flow-induced oscillations in an open cavity are illustrated in Figure 1. At the leading edge of the cavity, the boundary layer separates and forms a free shear layer. Disturbances in the free shear layer amplify and convect downstream, ultimately growing into large-scale vortical structures. In an open cavity, these coherent structures span the length of the cavity and impinge near the trailing edge corner of the cavity.

Krishnamurty (1955) was among the early researchers studying cavity flow. He used Schlieren imaging, interferometry, and hotwire measurements to examine the acoustic near field in the cavity and determined that the sound frequency was inversely proportional to the length of the cavity for a fixed depth. Roshko (1955) studied the cavity flow based on the hypothesis that a system of vortices exists in the cavity and drives the turbulence in the cavity. He concluded that a single, stable vortex forms in the cavity. He also used Schlieren imaging to show that the impingement of the shear layer on the aft wall is a source of sound waves. Rossiter (1964)

developed a semi-empirical model of the cavity flow which he was able to use to predict the resonant frequencies, or Rossiter modes, in the surface pressure signal. Rossiter's model is still the basis for predicting the frequency of the tones observed in resonating cavities. The review of Rockwell and Naudascher (1978) provides a good description of the level of understanding of cavity flow physics gained through many of the early studies. More recent experimental studies like Heller and Delfs (1996), Unalmis et al. (2001) and Zhuang et al. (2006), among many others, have shed light on the specifics of cavity flows in supersonic flows. In addition, the recent review article of Lawson and Barakos (2011) provides an extensive review of most of the literature published to date on high speed cavity flow applications.

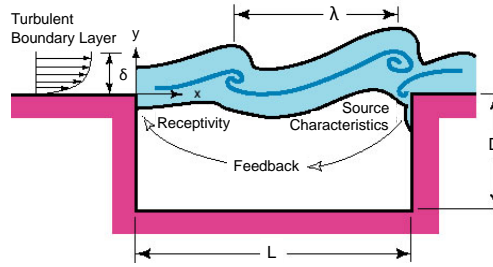


Figure 1: Flow-induced cavity resonance for an upstream turbulent boundary layer, adapted from Cattafesta et al, 2008.

1.2.1 Control of Cavity Flows

Techniques to suppress cavity oscillations can be classified in several ways. In this work, we choose the classification detailed in Cattafesta et al. (2008) to be consistent with terminology used in active noise and vibration control. Active control provides *external* energy (e.g., mechanical or electrical) input to an adjustable actuator to control the flow, while passive control techniques do not. Passive control of cavity oscillations has been successfully implemented via geometric modifications using, for example, fixed fences, spoilers, ramps, (Heller & Bliss, 1975 and Shaw, 1979) and a passive bleed system (Chokani and Kim, 1991). Note that some control devices considered passive by this classification extract energy from the flow itself and have been called '*active*' by other researchers. Pertinent examples include unpowered or passive resonance tubes (Stanek et al., 2000) and cylinders or rods placed in the boundary layer near the leading edge of the cavity (Mcgrath & Shaw, 1996, Ukeiley et al, 2004 and Dudley and Ukeiley, 2008). Active control methods include steady (Zhuang et al., 2006) and unsteady (Shaw, 1998) fluidic injection and zero net mass flux actuators (Lamp and Chokani, 1999), as well as mechanical devices such as piezoelectric flaps (Cattafesta et al., 1997). These have proven to be effective at reducing tones. The advantage of these active methods is that they can readily be paired with a closed loop controller to adapt the actuator to changing flow conditions. A large number of actuation methods have been examined, and the interested reader is referred to reviews such as Cattafesta et al. (2008) and Rowley and Williams (2006) for more details of available control methods.

Throughout this work we will use the injection of mass at the upstream end of cavity. Several different methods of this mass injection have been investigated. Vakili and Gauthier (1994) used a perforated plate upstream of the cavity to inject air into the approaching boundary layer. They reported a 27 dB reduction in the peak tones in the cavity and concluded that the mass injection altered the feedback in the cavity. Bueno et al. (2002) examined various length cavities in a Mach 2 flow subject to steady and pulsed blowing and found the steady blowing to

be more effective at reducing the surface pressure fluctuations. Zhuang et al. (2006) used leading edge microjets to alter the shear layer over the cavity. They were able to achieve a 20 dB reduction in the cavity tones and a 9 dB reduction in the broadband noise. They also used shadowgraph visualization and particle image velocimetry (PIV) to observe that the injection reduced the flow unsteadiness inside the cavity. In a precursor to the current study, Ukeiley et al. (2008) used both microjets and spanwise-aligned slots to control the cavity flow and reduce the fluctuating surface pressures. That study used a complex cavity geometry but found that the surface pressure spectra behaved very similarly to those of a rectangular cavity. The results presented showed a 55% reduction in fluctuating surface pressure levels on the aft wall of the cavity. Furthermore, reductions were seen in both the tonal and broadband components of the fluctuating pressures. It was also suggested that there is a link between surface pressure reductions and increased three-dimensionality of the features in the shear layer. This was based on the observation of significant reductions in the spanwise coherence of the surface pressure on the aft wall with leading edge blowing applied. One aim of the current work is to confirm this hypothesis through velocity field measurements. The experimental study reported in Ukeiley et al. (2008) was followed up by a numerical study of similar conditions reported in Arunajatesan et al. (2009). There the surface pressure reductions and some of the effects of the control on the flow in the cavity shear layer were reported. Specifically, it was noted that the spanwise coherence of turbulent structures was altered and the flow impinging on the aft wall was significantly more three-dimensional resulting in less flapping of the cavity shear layer. That study also noted an increase in the turbulence production in the initial part of the shear layer, and it was concluded that the primary effect of the leading edge blowing was the redistribution of the turbulent energy from larger to smaller scale vortical structures.

In addition to the open-loop control (OL) discussed above there has been some work on closed-loop (CL) adaptive control, which was also reviewed in Cattafesta et al. (2008). In some of the control methodologies, three-dimensional excitation is used at the leading edge to alter the cavity shear layer, which in turn affects the aft-wall source characteristics. Kegerize et al. (2007) used a piezoelectric bimorph actuator and the Generalized Predictive Control (GPC) method and successfully suppressed multiple Rossiter modes. However, there was no effect on broadband noise level. Cattafesta et al. (2008) suggested that fundamental and comprehensive studies on the cavity flow field and its response to open- and closed-loop control are needed to develop efficient and effective control strategies to suppress both the multiple Rossiter modes and broadband noise level simultaneously. One of the goals of this study is to understand the effects of open-loop and closed-loop control on cavity oscillation suppression of both tonal and broadband noises, with particular emphasis on three-dimensional forcing strategies. Specifically, open-loop control using sinusoidal excitation signals and adaptive closed-loop control, using quasi-static Downhill Simplex (DS) and dynamic ARMARKOV and GPC algorithms, are explored with a three-dimensional zero-net mass-flux (ZNMF) piezoelectric actuator array to suppress the unsteady pressure oscillations inside the cavity at Mach numbers of 0.3 and 0.4.

1.3 Objectives

The overall goal of this work is to develop an adaptive flow control methodology which can be used in supersonic flows over open cavities. To achieve this long range goal, there are several objectives which were addressed in this study:

- Investigate the effects of leading edge actuator configurations to more effectively reduce the fluctuating surface pressures in open cavity flows.

- Acquisition and analysis of detailed flow measurements in both uncontrolled and controlled (open- and closed-loop) compressible (subsonic and supersonic) cavity flows, including velocity field measurements with PIV and density field measurements with Schlieren techniques.
- Enhancement of adaptive control methodologies using spanwise segmented actuation schemes that incorporate the best features of open- and closed-loop control schemes to suppress both tonal and broadband noise..

1.4 Layout of this Document

In this document we will discuss our accomplishments during the course of this AFOSR grant, all of which are pieces that will allow for us to efficiently reduce the surface pressure fluctuations in open cavities in supersonic flows. We will first discuss the effects of steady blowing using spanwise segmented slots at the cavity's leading edge to show their efficacy at reducing the fluctuating surface pressure. This will include detailed flow measurements to show how the flow is affected. This will be followed by a discussion and presentation of results demonstrating several adaptive control strategies. Finally, we will summarize all of the results and put forth some direction that would be fruitful for future work.

2 Steady Blowing

As discussed in the introduction, one aspect of this study involved identifying effective leading edge slot configurations for reducing the fluctuating surface pressure and identifying some of the key flow features associated with them. In the following section we will detail applications of this to open cavities with both supersonic and subsonic free stream conditions.

2.1 Supersonic Application

2.1.1 Facility and Experimental Setup

The experiments conducted for this part of the effort were carried out at the Compressible Flow Facility at the University of Florida Research and Engineering Education Facility (UF-REEF). This facility has a floor mounted cavity and is designed to support surface pressure, Schlieren, and particle image velocimetry data acquisition methods.

2.1.1.1 Facility

The facility is a blowdown wind tunnel and is shown in Figure 2. The wind tunnel is supplied by a 44 m³ tank which stores dry air at 1240 kPa. Air flow through the wind tunnel is regulated with a 152 mm Fisher valve operated by a LabVIEW program. The program and valve combination are capable of maintaining the desired stagnation pressure of 172±4.6 kPa. After the control valve, the air passes into a stagnation chamber and then through a honeycomb section, a transition piece, and a nozzle. The nozzle is a two-dimensional converging-diverging nozzle that accelerates the flow to Mach 1.44. After the nozzle the air travels through the test section and then is exhausted outside the building. The average free stream dynamic pressure is 74.3 kPa. The approaching boundary layer height is 3.8 mm (99% of free stream velocity) and was determined to be turbulent based on its shape factor of 1.2, as detailed in Dudley (2010). The tunnel has a rectangular test section measuring 76.20 mm wide, 101.6 mm tall, and 254.0 mm long. Further details of the facility construction and characterization can be found in Dudley et al. (2008).

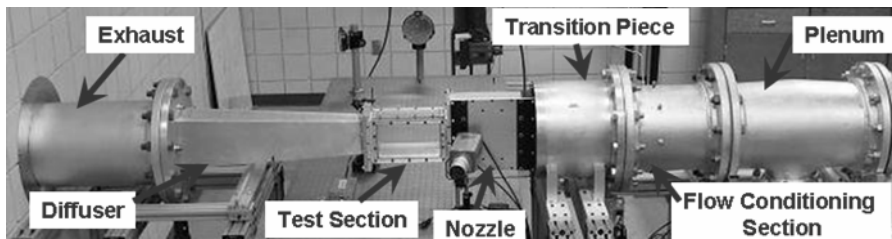


Figure 2: Photograph of UF-REEF supersonic wind tunnel

2.1.1.2 Cavity Model and Actuators

The cavity model was mounted in the floor of the test section and measured 76.20 mm wide, 76.20 mm long, and 12.70 mm deep, giving a length to depth ratio (L/D) of 6. The cavity spanned the full test section width to simplify the acquisition of optical data. The cavity was built with modular blocks to allow for it to be reconfigured as necessary for other studies, e.g. Dudley (2010). The current cavity configuration can be seen in Figure 3, along with the coordinate system referenced for this study. The blocks were machined out of 6061 aluminum

and treated with a Rhodamine paint to shift the wavelength of light reflected off the cavity surfaces in the PIV experiments.

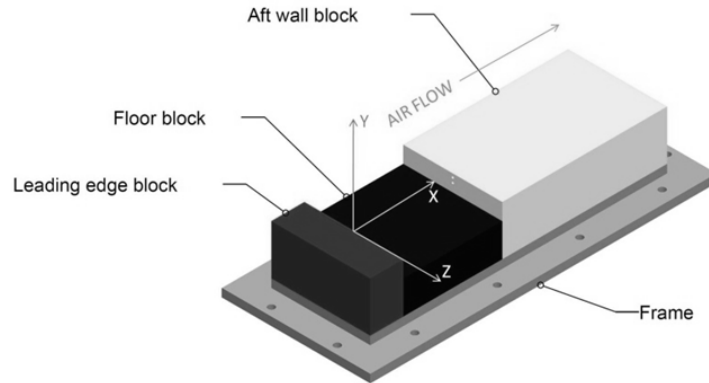


Figure 3: Cavity model with coordinate system

In order to alter the flow, rectangular slots were used to inject air normal to the free stream at the leading edge just before the cavity lip. Configurations of one, three, and five slots were tested and are shown in Figure 4. The dimensions of the configurations were determined primarily by fabrication constraints; however, the fabrication method allows for the assessment of different spanwise configurations without altering the slot thickness.

A compressed air line attached to the underside of the blocks was used to supply air to the slots. To allow for measurement of the stagnation pressure of the slot air a stagnation chamber was built into each block. An Alicat Scientific M-250SLPM-D mass flow meter with an accuracy of 0.8% was placed in the supply line and a Druck PMP 4015 pressure transducer was used to measure the stagnation pressure. During the PIV experiments, the mass flow meter had to be removed due to incompatibility with the oil seeder. For these experiments the flow rate was controlled by maintaining the stagnation pressure according to the data recorded during the surface pressure experiments

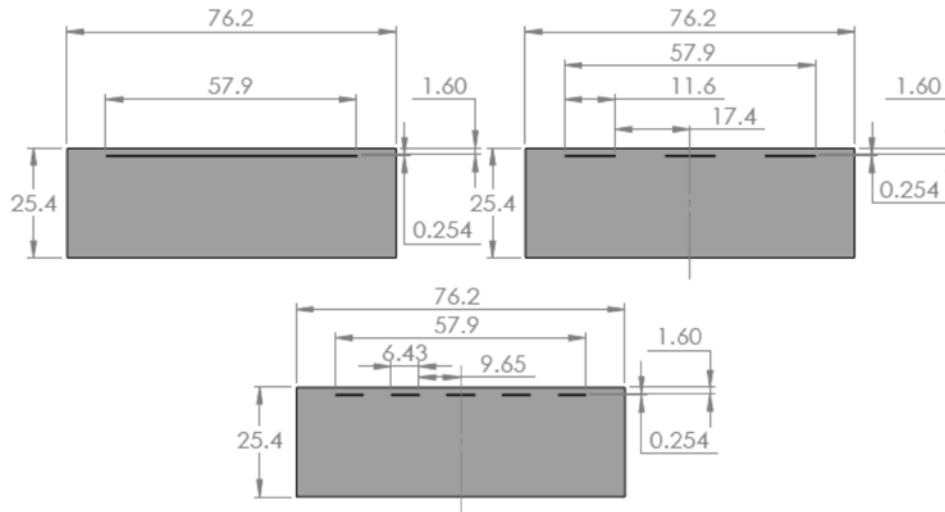


Figure 4: Top view of leading edge blocks showing slot configurations. Dimensions in millimeters

2.1.1.3 Fluctuating Surface Pressure

Surface pressure measurements were acquired using Kulite piezoresistive pressure transducers. The ones used in this study have a diameter of 1.7 mm and a sensitivity of approximately $2.5 \mu\text{V}/\text{Pa}$. For the current work, four transducers were installed on the centerline of the cavity, with three in the floor and one in the aft wall. Table 1 lists the model numbers, locations, and pressure ratings of the four transducers used. The transducers were sampled at 90 kHz for 5.8 seconds using a National Instruments PXI 4472 24-bit data acquisition card. In order to calculate the power spectral density (PSD) the data sets were broken up into records of 8192 points, giving a frequency resolution of 11 Hz and 64 averaging blocks. The PSD was calculated using Welch's method (Bendat and Piersol, 2000) with a Hanning window and no overlap.

Table 1: Pressure transducer details

Kulite Number	X/D	Y/D	Kulite Model	Rated Pressure
1	1.5	-1.0	XCQ-062-5D	5 PSID
2	3.0	-1.0	XCQ-062-5D	5 PSID
3	4.5	-1.0	XCQ-062-5D	5 PSID
4	6.0	-0.5	XCQ-062-30A	30 PSIA

2.1.1.4 Particle Image Velocimetry

Particle image velocimetry was used to obtain velocity vector fields at various locations in the flow for two different orientations. Two- and three-component data were acquired for laser sheet orientations aligned with the flow and perpendicular to it, respectively. A commercially available system from LaVision was used to acquire and analyze the data for this study. Details of this system will be given below.

For all of the experiments air flow was seeded with atomized droplets of Di-ethyl hexyl sebacate (DEHS), an oil that is commonly used for PIV experiments. A LaVision four-nozzle head submicron liquid particle generator was used to introduce particles on the order of $1 \mu\text{m}$ into the free stream flow. A Dantec 10F03 Seeding Generator, producing particles on the order of $2 \mu\text{m}$, was used to seed the slot airflow.

A Litron Nano L 135-15 Nd:YAG laser was used to illuminate the seed particles. This laser emits 532 nm light at 135 mJ per pulse. The laser was mounted above the test section. For two-component PIV, the laser optics were configured to cast a laser sheet approximately 1 mm thick into the cavity aligned in the flow direction. For three-component PIV the laser sheet was thickened to 3 mm and turned 90° so that the planes acquired were normal to the flow direction. Imager ProX-4M cameras, also supplied by LaVision, with a pixel resolution of 2048x2048 were used to acquire the images. For two-component PIV a single camera was fitted with a Nikon AF Micro-Nikkor 60 mm f/2.8D lens and set outside the test section and focused on the $z = 0$ plane looking normal to the laser sheet. In the three-component PIV setup, two cameras were fitted with Nikon AF Nikkor 50 mm f/1.4D lenses in a Scheimpflug arrangement and set up to look into the cavity at various x locations from opposite sides, each at an angle of 55° from the flow direction. For both applications the camera lenses were fitted with optical band-pass filters

centered at 532 nm. When coupled with the Rhodamine treatment of the cavity surfaces, this greatly reduced unwanted glare reaching the cameras.

DaVis 7.2 from LaVision was the software used to acquire data and process the images into vector fields. The software uses a cross correlation algorithm with 50% overlap and a 2-pass interrogation region, with the first pass being 64x64 pixels and the second being 32x32. According to Grant and Owens (1990), about 750 vector fields are required to achieve a statistical convergence error of less than 3%. Therefore, 1000 vector fields were acquired for two-component PIV and 1500 were acquired for three-component PIV. This ensured that a sufficient number of vectors would be available at every location in the plane after bad vectors and outliers were discarded. The DaVis software uses a spatial median filter between passes to account for some outliers. An additional outlier detection algorithm was applied after the vector fields were output from DaVis. A multivariate outlier detection (MVOD) algorithm was applied to further improve the quality of the vector fields. The algorithm was developed by Hubert and Van der Veen (2008), while Griffin et al. (2010) successfully applied it to velocity field data in an analysis similar to the one performed here.

2.1.2 Results

This section will discuss the results from baseline experiments which were run with no control (solid leading edge block) and contrast them with the cases which were run with each of the leading edge slot configurations. It will start with a discussion of the fluctuating surface pressure and then continue on to the velocity field measurements in each of the measurement planes discussed above.

2.1.2.1 Fluctuating surface pressure measurements

Fluctuating surface pressure data were acquired to assess the effectiveness of the various slot configurations at the surface locations detailed in Table 1. Measurements were acquired for the baseline case and compared with measurements from experiments with various levels of mass flow through each slot configuration. Specifically, twelve mass flow levels were tested, as detailed in Table 2.

Table 2: Mass flow rates

Configur- ation	Mass flows tested (kg/s *10 ⁻³)					
1-slot	0.487	0.989	1.47	1.96	2.45	2.98
	3.45	3.95	4.43	4.94	5.42	5.93
3-slot	0.485	0.970	1.47	1.98	2.47	2.95
	3.45	3.93	4.45	4.95	5.45	5.92
5-slot	0.485	0.977	1.48	1.97	2.46	2.97
	3.43	3.95	4.46	4.95	5.42	5.92

The first operation performed on the surface pressure data was to calculate the percent reduction of the root mean square (rms) pressure which has been defined as,

$$\% P_{rms} \text{ reduction} = \frac{100 * (P_{rms-initial} - P_{rms-final})}{P_{rms-initial}} \quad \text{Eq. 1}$$

This is plotted in Figure 5 against a momentum coefficient, C_μ . The momentum coefficient is used to non-dimensionalize the momentum flux through the slots and is given by

$$C_\mu = \frac{mV}{\frac{1}{2}\rho_\infty U_\infty^2 w \delta} \quad \text{Eq. 2}$$

Here m is the aggregate mass flow through the slots, V is the mean velocity of the air exiting the slots which was calculated knowing the slots exit Mach number and the stagnation temperature, ρ_∞ is the free stream density, U_∞ is the free stream velocity, w is the cavity width, and δ is the approaching boundary layer's height. It should be noted we have chosen to use the momentum in the approaching boundary layer to normalize the momentum that is coming out of the slots as has been used in Ukeiley et al. (2008) as the jets do not penetrate the boundary layer and will be working against the boundary layer momentum. Figure 5 shows similar trends for each slot configuration in that there is a definite threshold in C_μ where the leading edge blowing becomes effective and a point where increasing the mass flow rate no longer produces any additional benefit. The results demonstrate that the 5-slot configuration is the most effective at reducing the rms of the fluctuating surface pressure at the aft wall location in terms of the overall reduction levels for the least amount of added mass flow. The 5-slot configuration shows the most significant reductions of the three at 44%, compared with the 31% and 33% of the 1- and 3-slot configurations, respectively. Additionally the 5-slot case requires the least mass flow to reach its optimal suppression level. The 5-slot configuration requires 1.97×10^{-3} kg/s while the 3-slot requires 2.96×10^{-3} kg/s and the 1-slot requires 2.98×10^{-3} kg/s. However, the trends are somewhat different when looking at C_μ since the different exit areas will alter the exit velocity for identical mass flow rates. The 1- and 5-slot cases were nearly the same at 0.0130 and 0.0128, respectively, while the 3-slot case value was 0.0206 at its best suppression level.

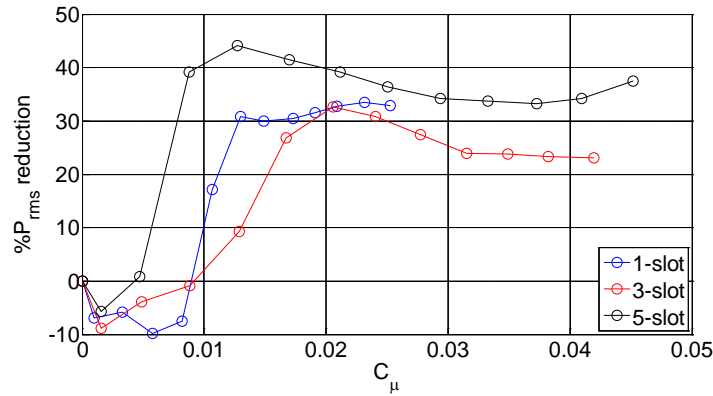


Figure 5: Pressure reductions for all blowing configurations

A more detailed assessment of the effectiveness of the control on the fluctuating surface pressure can be seen by examining the narrowband power spectra of the fluctuating surface pressure signals. Figure 6 compares the Power Spectral Densities (PSD) of the baseline at the aft wall location with those of the best blowing rate for each slot configuration. Plotted in this figure is the amplitude of the fluctuating pressure normalized by the free stream dynamic pressure. Additionally, vertical lines have been superimposed in the plots to represent the calculated values for the first six Rossiter modes using $\gamma=0.25$ and $\kappa=0.57$. Table 3 provides details of the slot flow for each of these blowing rates that were considered to be the best. The

mass flow rate, mass flow coefficient, mean slot exit velocity, and the ratio between the slot stagnation pressure and the free stream static pressure are presented. It is again clear that the 5-slot configuration is the most effective. The broadband levels are the lowest for this case, which is expected from the results presented in Figure 4 since the rms is equivalent to the integral of the PSD curve. Except for the peak associated with the second Rossiter mode in the 1-slot case, each peak is reduced to some extent in each configuration, with the 5-slot showing the best peak attenuation. Another noteworthy characteristic that these plots make clear is the shift in the dominant cavity tone. For the baseline case the third peak is the highest peak in the PSD plot. When the blowing is applied, this peak is reduced to a level below the second peak for each control configuration, thereby making the second peak dominant in the controlled flow.

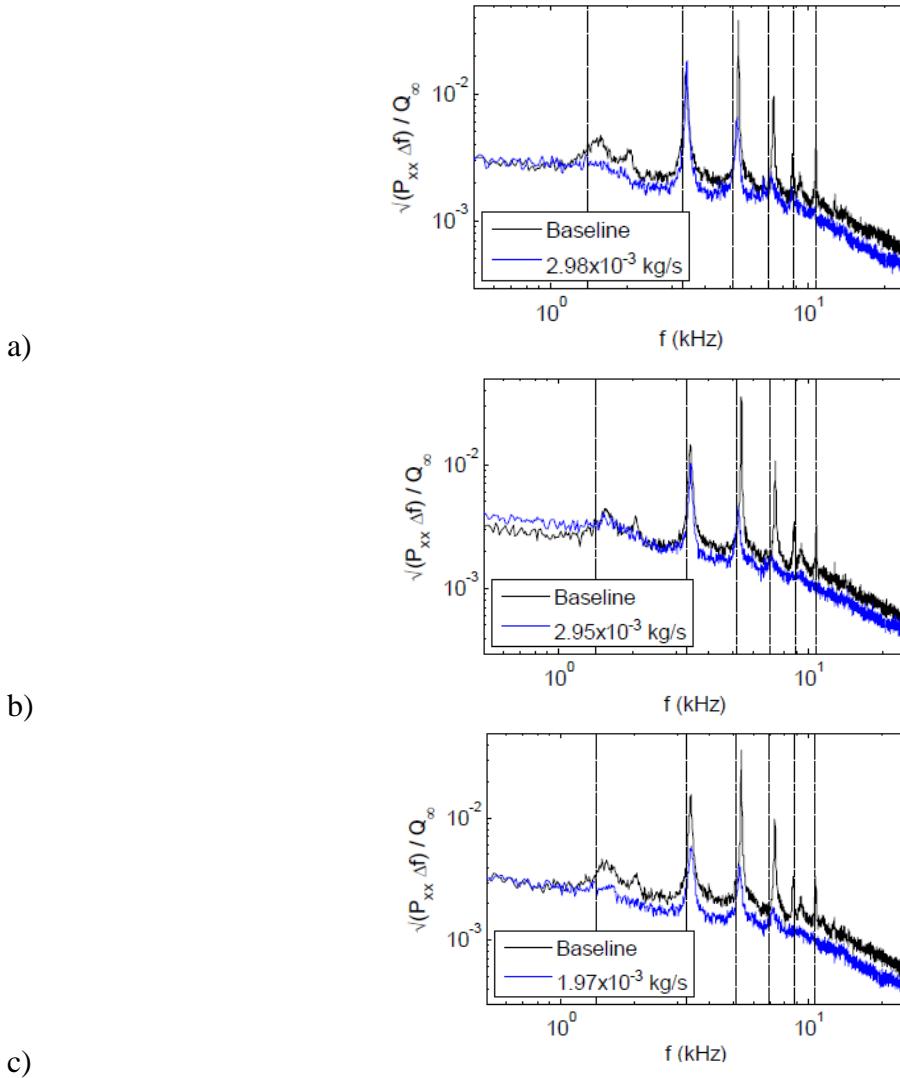


Figure 6: Power Spectra of fluctuating surface pressure on the cavity's aft wall for baseline and blowing configurations. a) 1-slot blowing configuration, b) 3-slot blowing configuration, and c) 5-slot blowing configuration

Figure 7 is a plot of the percent reduction of rms pressure at each floor location (as well as the aft wall location at $x/D = 6$, which is at $y/D = -0.5$) used with the most effective blowing rates for each of the slot configurations noted earlier. This shows that pressure levels are significantly reduced along the entire floor and not just on the aft wall. The 5-slot configuration showed the best attenuation at all of the floor locations. Finally, Figure 8 displays the ordinary coherence calculated as described in Bendat and Piersol (2000) for each configuration and sensor location. High levels of coherence at the resonance peaks are indicative of a highly correlated process in that frequency band. The plots show the coherence levels increased at all peaks for the 1-slot case but decreased for the 3- and 5-slot cases. For the 3- and 5-slot cases the coherence values at the frequency associated with the first Rossiter mode are nearly completely eliminated, implying the coherent flapping of the cavity shear layer is minimized by blowing with these slot configurations. Additionally, the coherence associated with the higher Rossiter modes (4 and greater) is no longer apparent over the broad-band levels for the 3- and 5-slot cases. Overall, the 5-slot appears to be the most effective as its coherence levels are more significantly reduced compared to the baseline case than the other slot configurations.

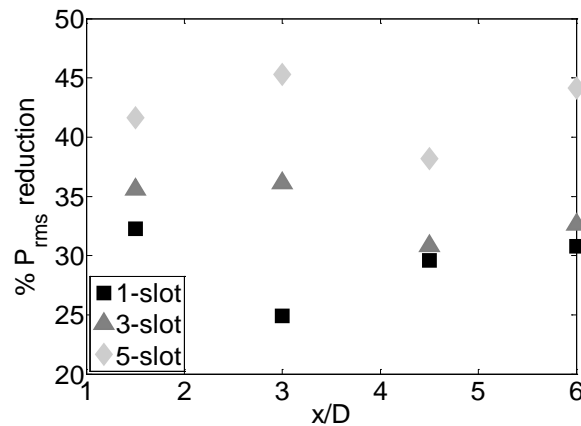


Figure 7: Reduction of rms values of the fluctuating surface pressure along the cavity surface.

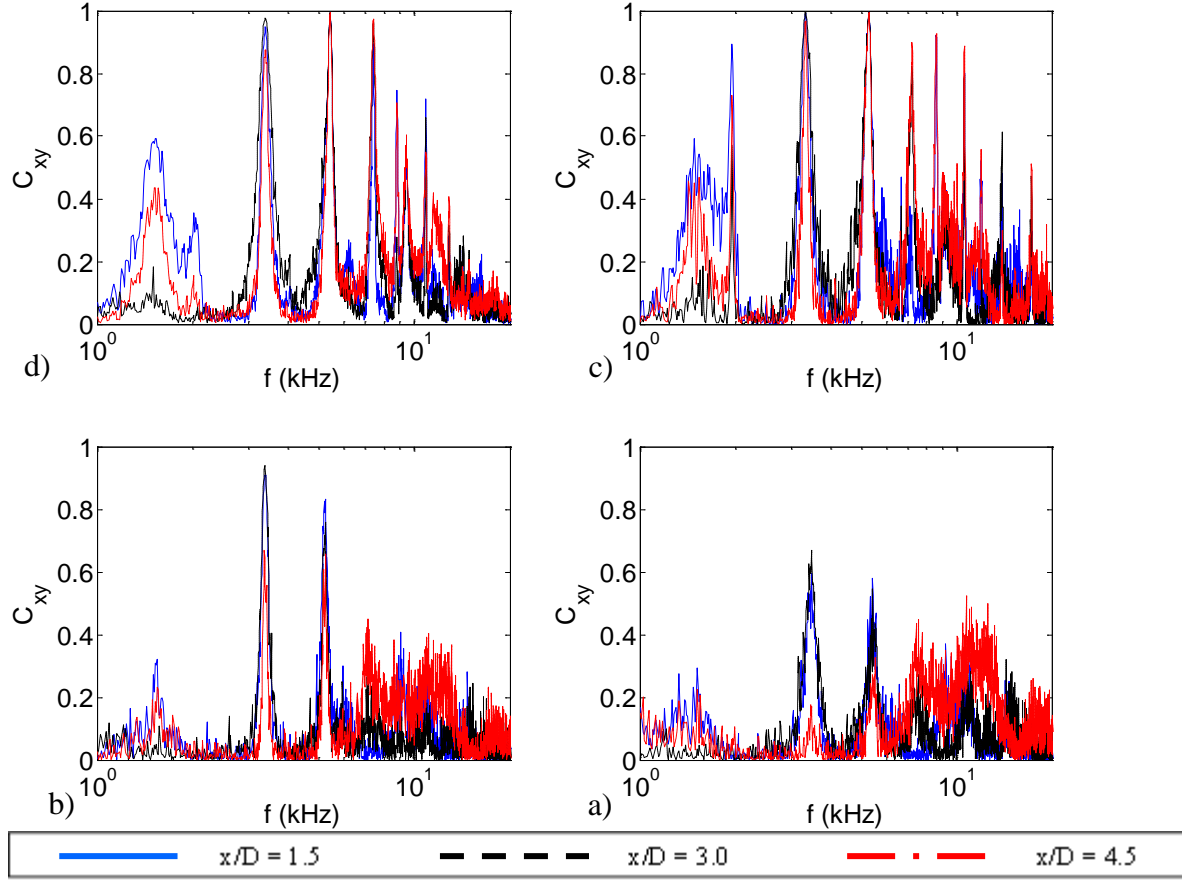


Figure 8: Ordinary coherence between the surface pressure signals on the floor and the aft wall. a) baseline configuration, b) 1-slot blowing configuration, c) 3-slot blowing configuration, and d) 5-slot blowing configuration

2.1.2.2 Streamwise Aligned Velocity Measurement Planes

Once the effectiveness of the leading edge blowing in controlling the fluctuating surface pressures was established, experiments were carried out using PIV to investigate the effect of control on the flow field. Due to the cumbersome nature of acquiring and storing PIV data, experiments were not run for all of the blowing cases tested in the surface pressure experiments. Instead, the results presented in Figure 5 were used to determine the most effective blowing rate for each slot configuration and velocity field measurements were acquired for the baseline configuration and the cases listed in Table 3.

Two-component velocity fields were acquired on streamwise aligned planes along the centerline location for each of the configurations. Data were also acquired at off-centerline planes for the 3- and 5-slot cases. The off-centerline locations corresponded to the middle of the gap between slots (i.e., locations of 17.4 and 6.43 mm from the centerline for the 3 and 5 slot configurations, respectively). Since the baseline and 1-slot cases were expected to produce roughly two-dimensional averaged flow fields, off-centerline planes were not acquired for those cases.

Table 3: Details of blowing cases for PIV measurements

	1-slot	3-slot	5-slot
\dot{m} (kg/s *10 ⁻³)	2.98	2.95	1.97
C_μ	0.0130	0.0205	0.0128
$P_{0,LE}/P_{FS}$	1.81	2.44	2.35

In the plots for the two-component PIV data, the airflow is from left to right and the cavity outline has been marked for reference. A small strip has been masked on the floor where glare due to oil buildup interfered with the image quality

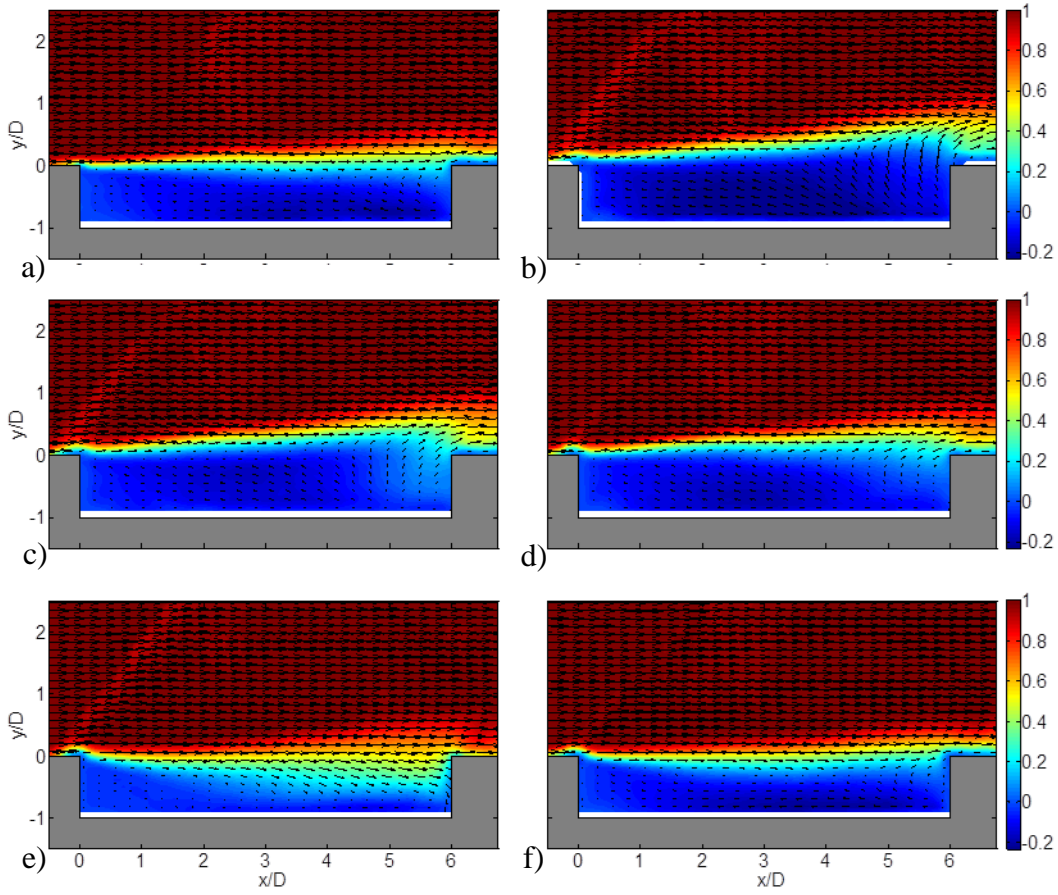


Figure 9: Streamwise mean velocity fields. a) Baseline configuration; b) 1-slot blowing configuration, centerline; c) 3-slot blowing configuration, centerline; d) 5-slot blowing configuration, centerline; e) 3-slot blowing configuration, off-centerline; and f) 5-slot blowing configuration, off-centerline

The mean streamwise velocity fields are presented in Figure 9. The plots consist of contours of mean streamwise velocity normalized by the free stream velocity with vectors

overlaid representing the u and v velocity components. In these plots the shear layer at the lip line of the cavity ($y/D = 0$) is clearly visible. The mean circulation can also be seen in the cavity as evidenced by the reverse flow along the floor of the cavity. On the centerline planes in the controlled cases (Figure 9 b-d), the shear layer is lifted up above the $y/D = 0$ line so that, in a mean sense, the full shear layer does not impinge on the aft wall as it does in the baseline case. This lifting is present but somewhat less so in the 5-slot case due to the lower mass flow through the slots. The controlled cases also show evidence of a stronger shock that forms near the leading edge of the cavity. In the controlled cases on the centerline, the shock forms just upstream of the slots and is caused by the blockage where the slot air meets the free stream air. The shock is strongest for the 1-slot case, as is apparent by the greater velocity defect, due to the greater spanwise coverage of that configuration.

The off-centerline plots in Figure 9e) and f) show trends contrary to those observed on the centerline plane. Instead of being lifted above the cavity mouth, the shear layer dips down further into the cavity for the controlled cases than for the baseline case. As will be shown in the three-component PIV results, this effect is due to streamwise-aligned vortical structures created by the interaction between the free stream air and the slot air. These structures act to push the air up behind the slots and down between them, as shown here in the streamwise aligned measurement planes.

The vorticity thickness was calculated as a measure of the shear layer thickness using an incompressible formulation in the same manner as Murray et al. (2009) as there was no measurement available of the density field. In this formulation, the vorticity thickness is defined as,

$$\delta_{\omega} = \frac{U_{\infty}}{(\frac{\partial U}{\partial y})_{max}}. \quad \text{Eq. 3}$$

According to Brown and Roshko (1974) the streamwise vorticity thickness growth is expected to be around 0.162 for a turbulent free shear layer. Cattafesta et al. (1997) studied a subsonic cavity flow with a turbulent boundary layer and found linear spreading rates near that value. The baseline data in the present study roughly match with a value of 0.128 which is also consistent with the measurements of Murray et al. (2009). The spreading rate is somewhat lower than the previous studies mentioned, which is to be expected for a supersonic flow. The vorticity thickness calculations for all cases on the centerline plane are presented in Figure 10 a), and the off-centerline calculations are presented in Figure 10 b). All of the vorticity thickness plots presented here have been normalized by the value measured in the boundary layer just before the cavity lip. Beginning with the centerline data, the curves show the thickness for the blowing cases to be 20% higher than for the baseline in the first 10-15% of the cavity in the axial direction. However, the slopes of the curves given by the blowing cases are lower than those of the baseline case so the values cross just before the midpoint in the cavity. The data show roughly linear behavior except for the 5-slot curve, which has a definite increase in slope near the midpoint in the cavity. The 3-slot curve also shows this feature but not until much later, at around $x/D = 5$. The 3- and 5-slot vorticity thicknesses behave much differently at the off-centerline planes. The 3-slot curve still shows the slope increase but it is now at the midpoint in the cavity. The curve levels off at around $x/D = 4.5$. The 5-slot curve becomes less steep at the midpoint in contrast to the centerline plane which showed the slope becoming steeper at this point.

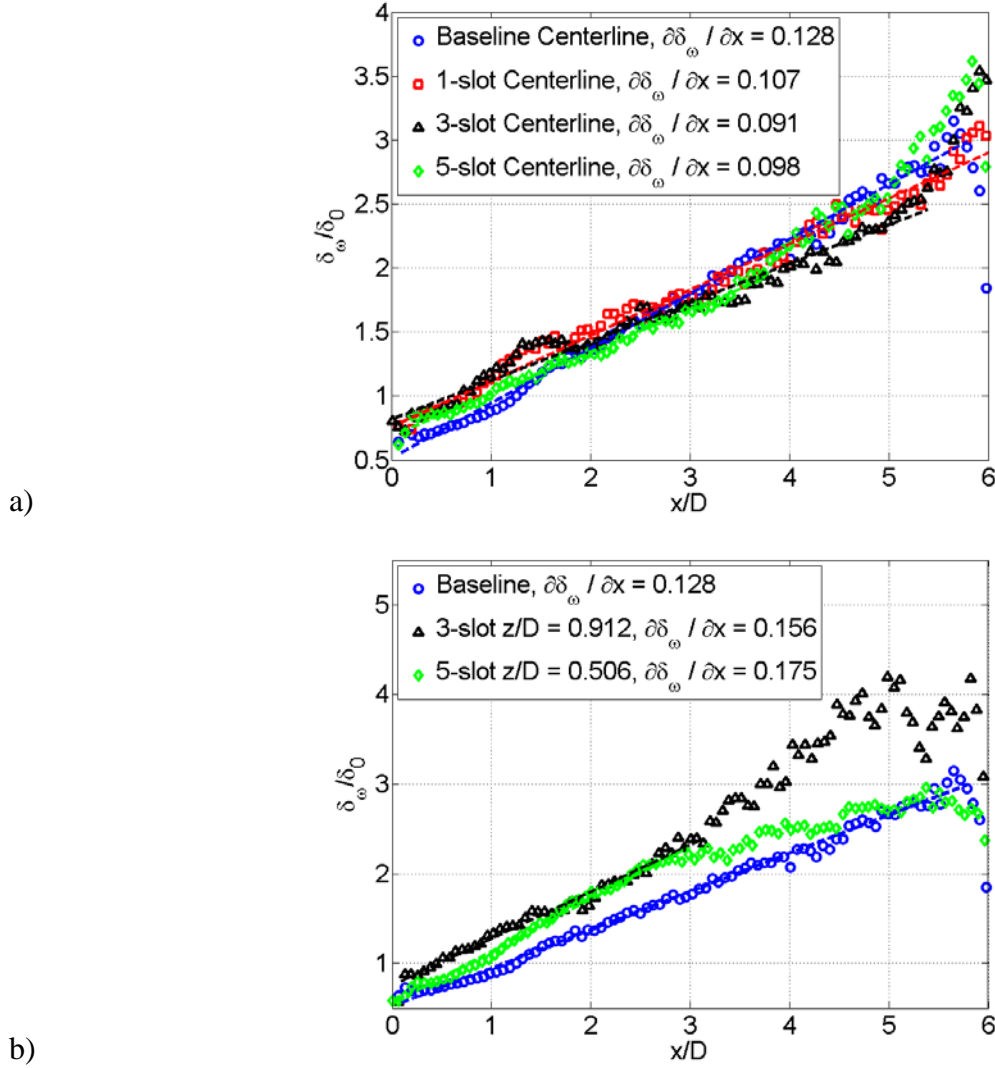


Figure 10: Vorticity thickness. a) Centerline plane and b) off-centerline plane

The transverse component of the fluctuating velocity fields shown in Figure 11 emphasizes the behavior of the shear layer observed in the plot of the mean streamwise velocity. The values in these plots are also normalized by the free stream velocity. For the centerline cases the shear layer is lifted so that the highest fluctuating values are above $y/D = 0$. The fluctuating values also appear to be slightly increased from the baseline case, which is consistent with the results of Arunajatesan et al. (2009). The effect is less evident for the 5-slot case, but the trends are still present. Another characteristic that can be observed from these plots is the earlier development of the shear layer for the controlled cases. This is seen by the contours of higher fluctuations reaching farther upstream in the cavity for the controlled cases than for the baseline case. The off-centerline planes again show the shear layer dipping lower into the cavity, as seen in Figure 11 e) and f). It also grows faster than in the baseline case, as seen in the centerline data. The overall fluctuating magnitudes in the controlled cases are similar to those of the baseline case but the regions of higher fluctuation are spread out over more of the cavity for the controlled cases.

One component of the Reynolds Shear Stress (RSS) was calculated to give a more complete picture of the turbulence in the cavity and is presented in Figure 12. As with the fluctuating velocity fields, these plots show the highest levels of turbulence being pushed up out of the cavity on the centerline for the controlled cases. The 3- and 5-slot controllers also have the effect of reducing the overall levels of RSS while the 1-slot increases the levels. For the off-centerline planes the levels are also decreased, with the 3-slot case showing the most significant reduction of RSS levels of all of the cases presented. The regions of high turbulence are deeper in the cavity as is expected for the off-centerline planes, but the levels for both controlled cases are less than for the baseline case.

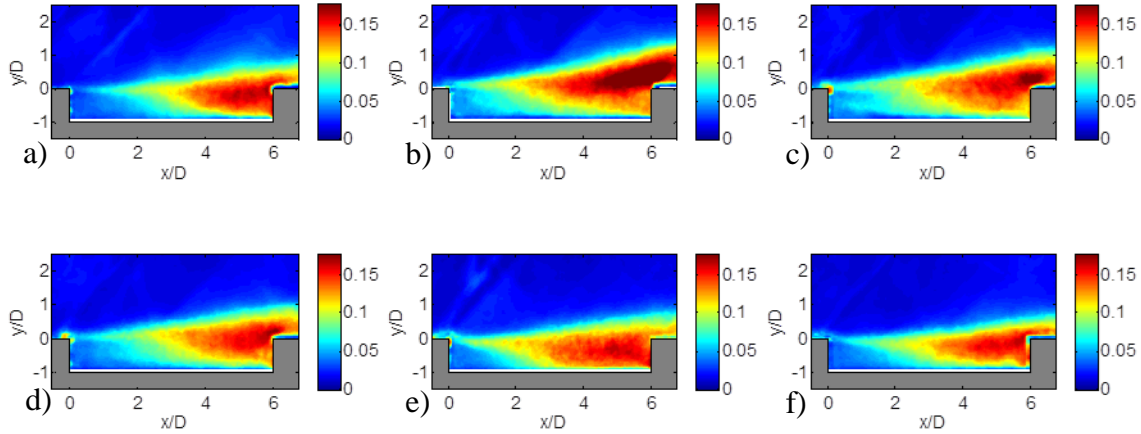


Figure 11: Transverse fluctuating velocity fields. a) Baseline configuration; b) 1-slot blowing configuration, centerline; c) 3-slot blowing configuration, centerline; d) 5-slot blowing configuration, centerline; e) 3-slot blowing configuration, off-centerline; and f) 5-Slot blowing configuration, off-centerline

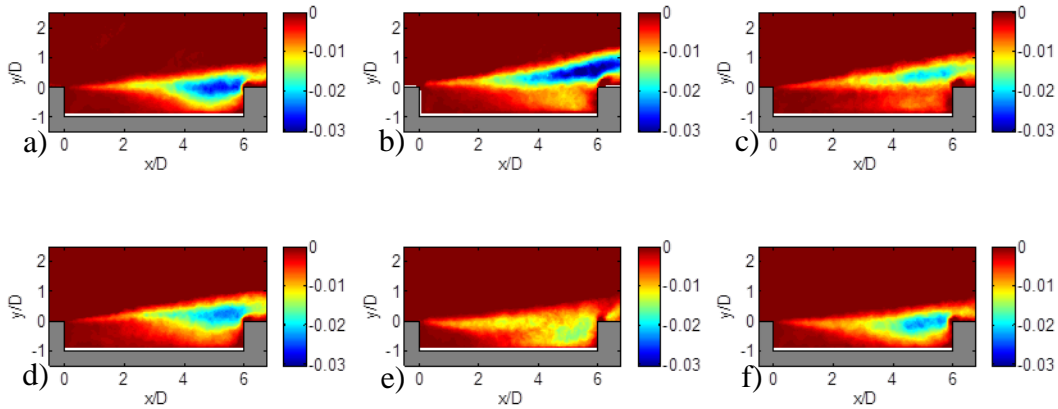


Figure 12: Reynolds Shear Stress. a) Baseline configuration; b) 1-slot blowing configuration, centerline; c) 3-slot blowing configuration, centerline; d) 5-slot blowing configuration, centerline; e) 3-slot blowing configuration, off-centerline; and f) 5-slot blowing configuration, off-centerline

2.1.2.3 Cross-Stream Aligned Velocity Field Measurement Planes

Stereoscopic PIV was used to acquire three-component velocity fields in planes perpendicular to the streamwise direction. These planes were located at $x/D = 1, 2, 4$, and 5 and covered nearly the entire span of the test section. As with the two-component data, the regions near the walls were blurred in the raw images due to glare and oil buildup so a small strip has been masked out in these plots. The plots are presented to the ends of the slots instead of all the way to the side walls because wall effects obscure the PIV images near the side walls. An insert showing the slot configuration is included at the bottom of each plot for easy reference. Planes were acquired for the baseline case and for the 3- and 5-slot configurations.

The mean velocity fields are presented first in Figure 13. These plots consist of contours indicating the streamwise component of velocity with vectors overlaid to indicate the transverse and normal components. The values are normalized by the free stream velocity.

The baseline plots reveal little spanwise variation in the front half of the cavity. The shear layer progresses in accordance with the data from the streamwise-aligned planes shown in Figure 8. The plots in the back half of the cavity show dips in the shear layer at about the $z/D = \pm 1.5$ locations. There are also slight recirculating regions associated with these dips. The last characteristic to note about these plots is the region of downward flow around the centerline near $y/D = 0$ at the $x/D = 5$ location. This is indicative of a large recirculation pattern in the cavity consistent with the measurements of Murray et al. (2009) in a transonic cavity and Zhuang et al. (2006) in a Mach 2 cavity.

The plots from the 3-slot configuration exhibit a spanwise waviness in the shear layer caused by the injection jets. The peaks correspond to the slot locations, and the dips correspond to the gaps between slots as can be seen from the slot locations denoted at the bottom of the figures. This accounts for the behavior of the shear layer observed in the streamwise-aligned measurement planes, where the shear layer was lifted at the centerline planes and depressed at the off-centerline planes. The amplitude of the spanwise pattern grows as it moves downstream. At the furthest downstream measurement location in the cavity, strong recirculation regions are visible at the edges of the middle slot with the center of rotation at approximately $y/D=0$. This confirms the earlier statement that vortical structures are created by the slot blowing and are responsible for the behavior of the shear layer. The structures rotate away from the slot which forces the shear layer up behind the slots and down between them. This also creates a strong outflow at the centerline, in contrast with the downward flow seen at that location in the baseline case. The rotational regions are also present around the outside slots but they are less clear than those at the center slot, presumably due to interference from the test section side panels.

The 5-slot configuration shows similar behavior. The waviness of the shear layer is present and once again the peaks of the patterns correspond to the slot locations. The rotation region is also evident at the $x/D = 5$ location, though it is not as strong in this case and it is located further inside the cavity ($y/D \sim -0.4$) compared to the 3-slot case. There is another significant difference between the 3- and 5-slot cases in that the patterns in the shear layer become less sharply defined as the planes move downstream for the 5-slot case.

The differences between the 3- and 5-slot cases are explained by the slot spacing. The slots are farther apart in the 3-slot configuration, so the vortices created by the slot/free stream interaction have more time to develop before they spread and begin interfering with each other. From the plots presented in Figure 13, it appears that the vortices travel all the way to the aft wall without significant interference. The slots in the 5-slot configuration are closer together, meaning the vortices start out closer together and interact sooner. Indeed, just after the midpoint

of the cavity length they begin to interfere with each other. By the last measurement location in the cavity they have largely coalesced, and the flow pattern looks similar to the 3-slot cases with weaker rotational patterns.

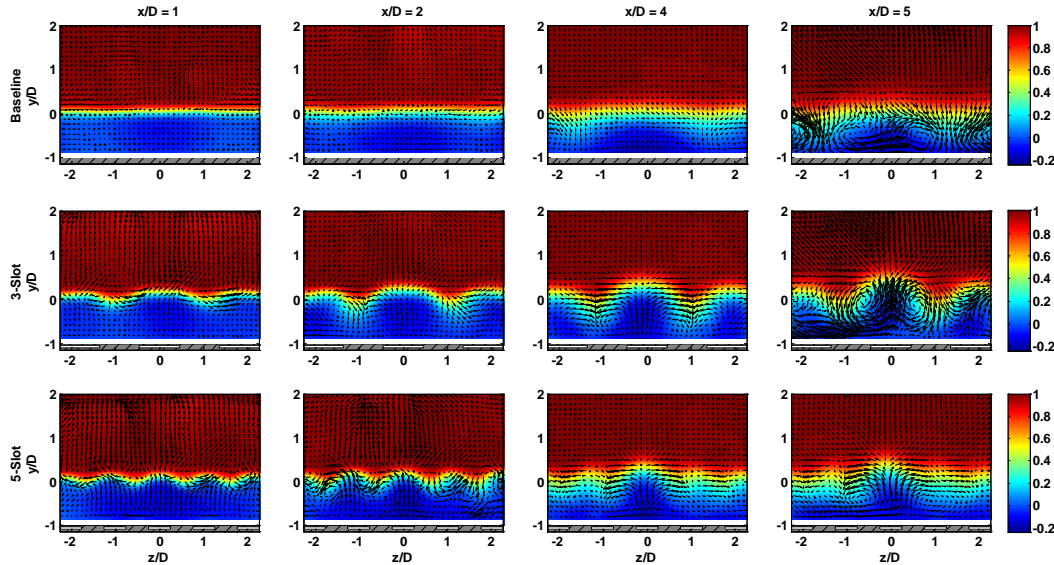


Figure 13: Mean velocity fields from cross-stream plane measurements. Velocity vectors of in-plane velocity components superimposed on out of plane velocity contours.

The transverse component of the fluctuating velocity is plotted in Figure 14. The streamwise and transverse components show similar trends, therefore only the transverse component will be discussed. The values plotted in this figure are again normalized by the free stream velocity.

The baseline case evolves as expected as the measurement plane moves downstream. In the front half of the cavity, areas of somewhat higher fluctuation levels are present at the ends of the shear layer, at $z/D \leq -2$ and $z/D \geq 2$. The dips observed in the shear layer in the mean velocity plots show up here as areas of lower levels of the fluctuating velocity. At the $x/D = 4$ and 5 locations the areas of highest fluctuation are inside in the cavity, in agreement with the corresponding streamwise aligned velocity plane measurements.

The stationary spanwise waves in the shear layer are apparent in the 3-slot case. The patterns themselves appear to contain the highest fluctuations, with the area under the patterns also experiencing high fluctuating velocities. The 3-slot configuration creates significantly higher fluctuating velocities than the baseline at all locations in the cavity, especially near the cavity centerline. This conflicts with the results of the RSS calculations from the 2-component PIV data that indicated the 3-slot to be the most effective at reducing turbulence levels in the cavity. As with the mean velocity, discrete patterns are visible all the way to the end of the cavity.

The transverse fluctuating velocity for the 5-slot case also shows the shear layer patterns in the first two locations in the cavity. As with the mean velocity plots for this configuration, the patterns coalesce after the midpoint in the cavity. The levels of fluctuating velocity in the cavity are much lower in the 5-slot case than in the 3-slot case at every location. The fluctuations are

also much lower than the baseline case in the back half of the cavity, with the front half planes showing little difference.

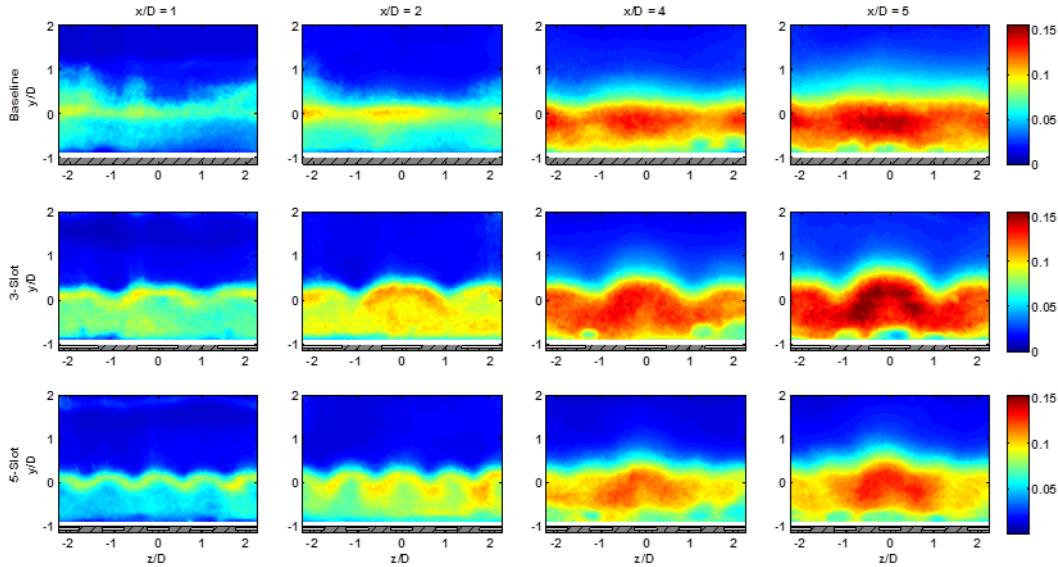


Figure 14: Transverse fluctuating velocity fields from cross-stream plane measurements.

2.1.3 Summary

Experiments were performed on supersonic flow ($M=1.44$) over an open cavity to assess the effects of leading edge slot blowing on the velocity field within the cavity. Specifically, three leading edge spanwise-aligned slot blowing configurations were examined in terms of their effects on the surface pressure and flow field. The results demonstrate how the most effective cases introduced a large amount of three-dimensionality into the flow field, altering the streamwise evolution of the cavity shear layer.

The fluctuating surface pressure measurements showed that all three slot configurations tested were effective at reducing both the tonal and broadband components of the fluctuating pressure signal. All of the configurations showed the trend of having little effect until the blowing rates exceeded a threshold, and then the control effectiveness saturating quickly after that point. The 1-slot configuration was the least effective of the three tested. While it achieved a similar level of overall suppression to the 3-slot configuration (just over 30% reduction) with a lower momentum coefficient, it was significantly less effective at reducing the peak pressure tones. The 5-slot configuration was the most effective at reducing the levels of the fluctuating surface pressure throughout the cavity with aftwall reduction levels over 40%. This configuration showed the most suppression while using the lowest mass flow through the slots to achieve its optimal suppression level. The 5-slot configuration was also effective at breaking up the resonant features of the fluctuating surface pressures, as evidenced by the results of the coherence analysis presented in Figure 8.

The two-component velocity fields aligned in the streamwise direction helped to provide understanding of the global alteration to the flow field caused by the blowing. The most significant result from these plots is the observation of the shear layer being lifted on a slot mid-plane and depressed between the slots by the blowing. This effect was not present in the 1-slot

case because the single continuous slot was not capable of inducing three-dimensionality to the flow in the same way as the segmented configurations. This explains the decreased effectiveness of the 1-slot configuration seen in the surface pressure analysis. The three-dimensional effects created by the 3- and 5-slot configurations alter the interaction of the shear layer with the aft wall which in turn changes the resonant features of the pressure signal. Since less of the shear layer impinged on the aft wall on the centerline, the feedback loop was presumably less powerful. This accounts for the reduced pressure levels observed on the cavity centerline.

The fluctuating velocity and Reynolds stress were helpful in observing the changes in the turbulence levels throughout the cavity. They showed the 3-slot to be the most effective at reducing the Reynolds stress ($u'v'$) levels in the cavity both on the centerline and at the off-centerline location. The 5-slot also showed reduced turbulence levels. The 1-slot actually increased the levels of RSS in the flow but the highest levels were pushed up out of the cavity by the blowing.

The velocity fields measured in cross stream aligned planes with the three-component PIV configuration revealed streamwise aligned vortical structures which account for the shear layer behavior discussed above for the 3- and 5-slot cases. The structures rotated such that the flow was forced up behind the slots and down between them. These structures helped to break up the large scale turbulent features in the shear layer and caused increased mixing with the free stream flow which, along with the lifting of the shear layer at the centerline, weakened the impingement of the shear layer on the aft wall. The fluctuating components helped to complete the picture of the behavior of the turbulence in the cavity. The transverse fluctuating velocity disagreed with the RSS plots in that the 3-slot configuration produced higher fluctuations in the cavity than the baseline while the 5-slot reduced the fluctuations.

2.2 Subsonic Application

In further studies to investigate the effects of the leading edge slot configurations additional studies were conducted with free stream Mach numbers ranging from 0.3 to 0.7. The studies presented in this section concentrating on including the effects of spanwise versus streamwise orientation of the leading edge slots on the fluctuating surface pressure.

2.2.1 Facility and Experimental Setup

The experimental setup for this phase of the study is briefly described in this section. The cavity oscillation control experiments are conducted in a subsonic blowdown wind tunnel with a test section composed of an integrated cavity model and a steady blowing jet actuator at its leading edge. The square test section, as shown in Figure 15, measures 2" by 2".

The rectangular cavity model has a length of $L = 127 \text{ mm}$, depth of $D = 25.4 \text{ mm}$, and full-span width of $W = 50.8 \text{ mm}$. The cavity length-to-depth ratio is $L/D = 5$. The cavity model is assembled with an acoustical treated ceiling or rigid ceiling. The flush-mounted acoustic treatment plate which enables simulation of the unbounded cavity flow encountered in a weapons bay is used as the wind tunnel cavity ceiling. The acoustic treatment consists of a porous metal sheet (MKI BWM series, Dynapore P/N 408020) backed by 50.8 mm thick bulk fiberglass.

Three pressure transducers (Kulite XT-190 series) are used to measure pressure fluctuations. One pressure transducer is located at the leading edge corner, one is located at trailing edge corner, and the third one is located in the center of the aft wall, as shown in Figure 15. For spectral analysis, the signals from the transducers are passed through a high pass

amplifier and then acquired using a NI PXI-1042Q data acquisition system (DAC) at a sampling rate of 65536 Hz. The spectra shown in this paper are computed using $\Delta f = 16$ Hz, 75% overlap with a Hanning window, and 100 block averages.

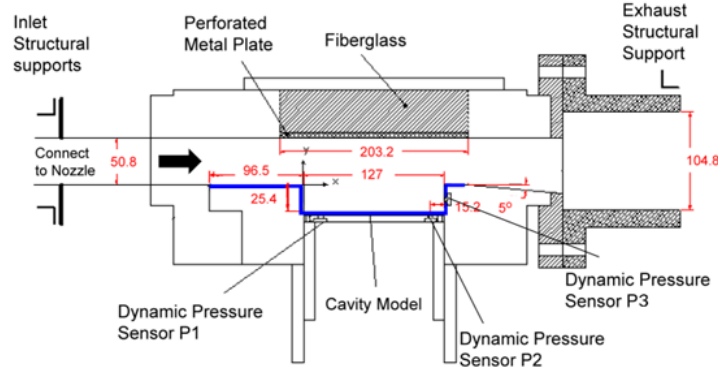


Figure 15: Schematic of the test section and the cavity model (Units in mm).

A compressed air line of 90 psi was attached to the underside of the actuator to supply air to the slot(s). An ALICAT M-250SLPM mass flow meter is used to measure the mass flow rate went through the actuator during the experiments. The stagnation pressure of the actuator chamber is measured by HEISE PM with a 30 psi module and the stagnation temperature is measured by an OMEGA thermocouple. The flow properties of the injection flow are acquired with the pressure data simultaneously.

The jet actuator mounted at the leading edge of the cavity consists of a cavity volume and a slot plate, as shown in Figure 16. Five spanwise slot plates and four streamwise slot plates were tested. The geometry of each slot plate is tabulated in Table 4.

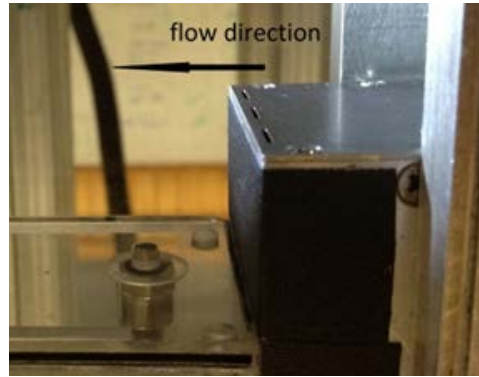


Figure 16: Photograph of slot plate and actuator.

Table 4: Slot dimensions for subsonic steady blowing exp.

Number of slots	1	3	5	7	9
L(mm)xW (mm)*	38.1x0.75	7.6x0.75	4.23x0.75	2.93x0.75	2.24x0.75

*L and W are the length and width of a single slot

After a general discussion of the fluctuating surface pressure reduction in the next section, we will highlight some of the flow features present in a subset of the slot configurations through the use of Schlieren imaging. The work presented will discuss the spanwise 3-slot plate and streamwise 3-slot plate. Detailed geometry of these slot plates are shown in Figure 17. We are concentrating on results from these two configurations as they yielded the best results from previous investigations and will allow us to directly examine the effects of slot orientation.

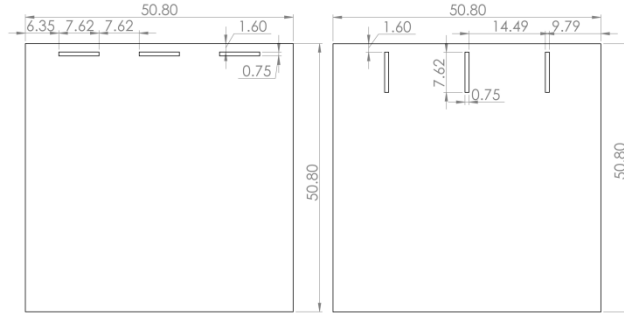


Figure 17: Subsonic slot configurations. Dimensions in millimeter.

2.2.2 Results

Figure 18 shows the results for the open-loop steady blowing control at Mach 0.3 to 0.7 using spanwise 3-slot plate. In particular, spectra of the fluctuating surface pressure on the aft wall are presented. The peaks seen in this figure for the baseline uncontrolled cases are due to the well-known Rossiter modes. Clearly, in these figures one observes the desired result, suppression of both the broadband and tonal components of the fluctuating surface pressure.

The results of the percent reduction of the rms pressure on the aft wall for different slot plates at a variety of flow velocities are shown in Figure 19 through Figure 23 for free stream Mach numbers ranging from 0.3 to 0.7. These results suggest the existence of an optimal slot geometrical arrangement to suppress cavity flow oscillations. We found that the jet actuator with three spanwise slots performs the best of those investigated in the subsonic application in suppressing the cavity oscillations, as shown in Figure 22 and Figure 23. Approximately 40% to 50% reduction of the pressure fluctuations are obtained at Mach 0.3 to 0.7 for the higher values of C_{μ} . The jet actuator with five spanwise slots also performs well, but more mass injection is required at the higher values of the free stream Mach number than for the spanwise 3-slot.

Table 5: Mass flow rate requirement for most effective control cases of spanwise 3-slot plate

Mach number	0.3	0.4	0.5	0.6	0.7
% P_{rms} reduction	36.3	41.8	45.4	52.9	50.6
C_{μ}	0.19554	0.16703	0.19355	0.23566	0.1713
\dot{m} (kg/s)	0.00199	0.00211	0.00321	0.00433	0.00435

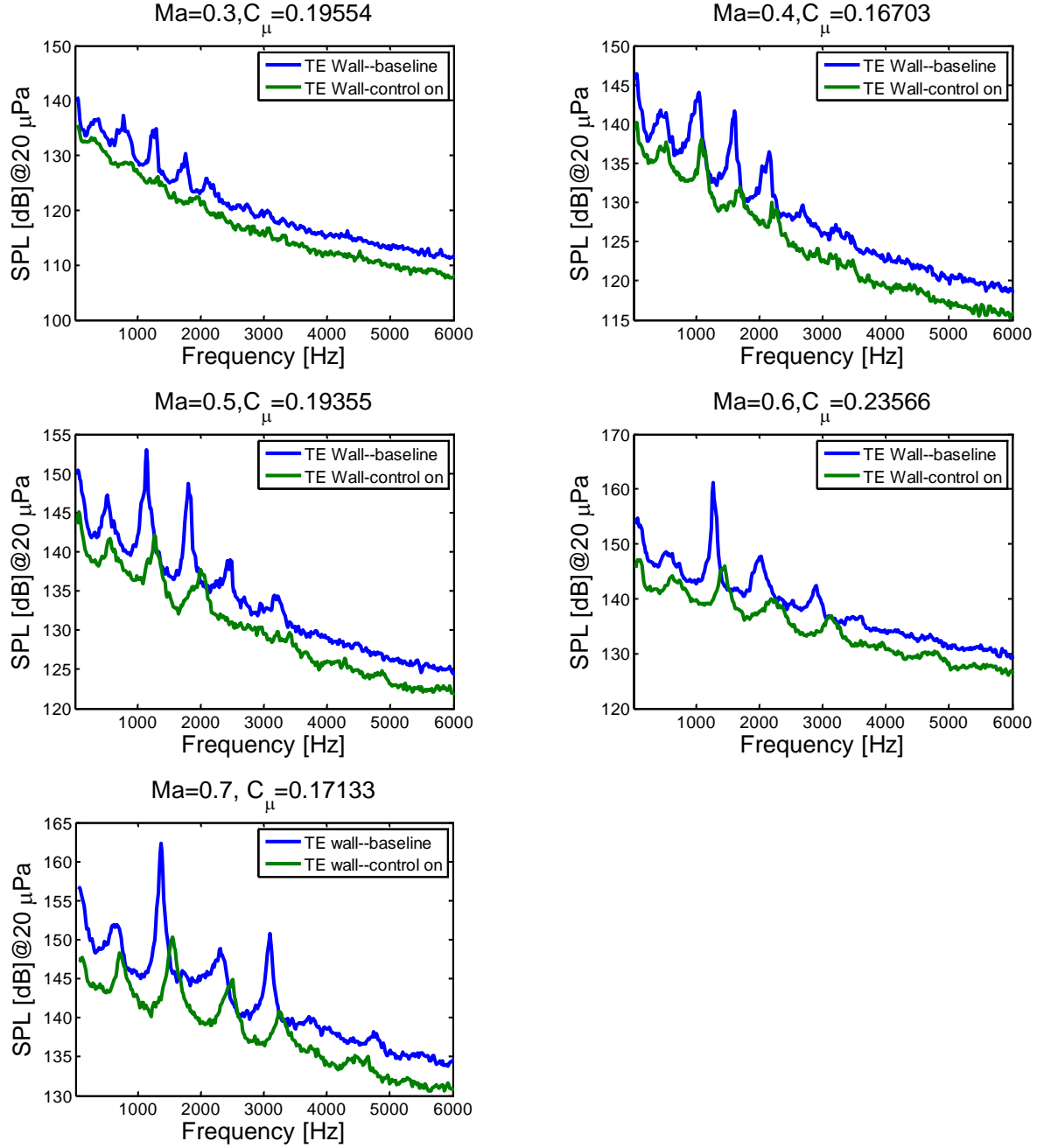


Figure 18: Aft wall spectra of most effective steady blowing cases for the spanwise 3-slot plate.

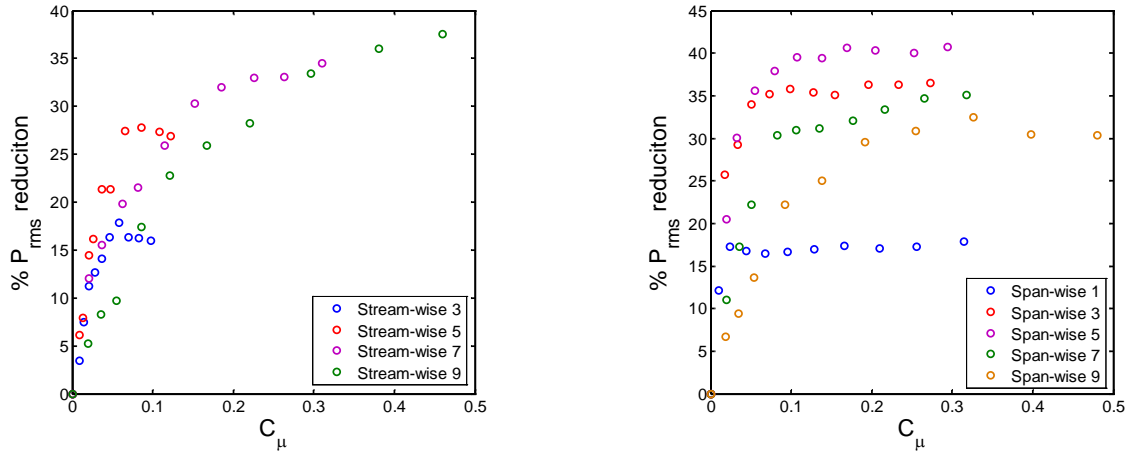


Figure 19: Mach 0.3, fluctuating surface pressure reduction at the aft wall.

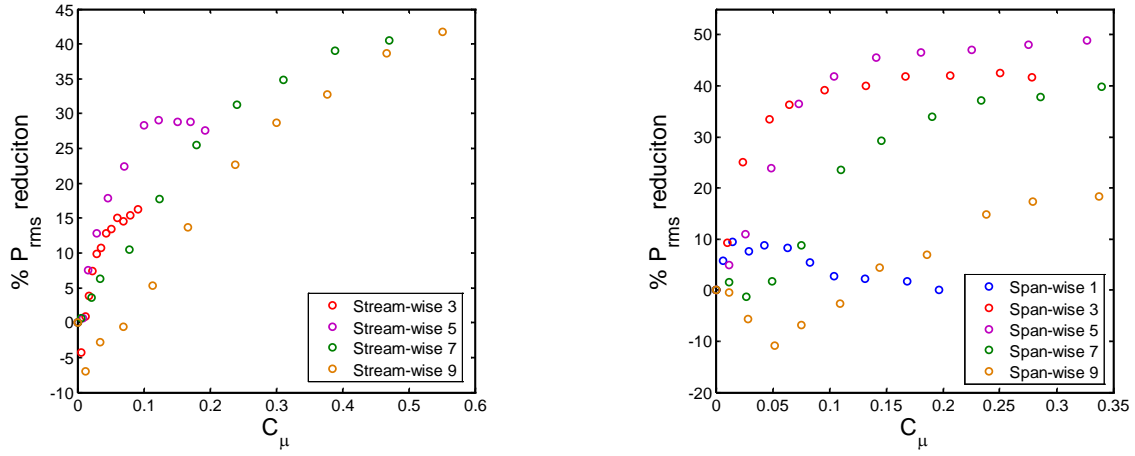


Figure 20: Mach 0.4, fluctuating surface pressure reduction at the aft wall.

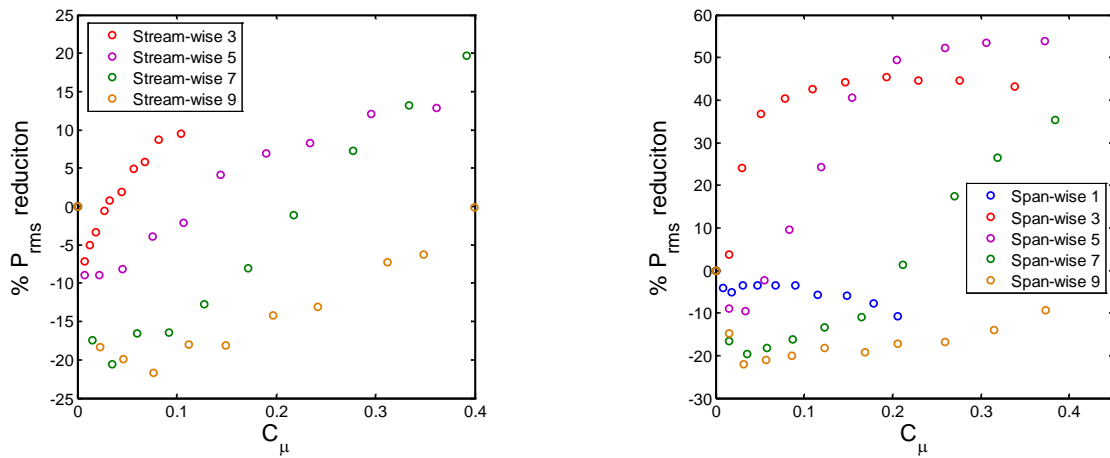


Figure 21: Mach 0.5, fluctuating surface pressure reduction at the aft wall.

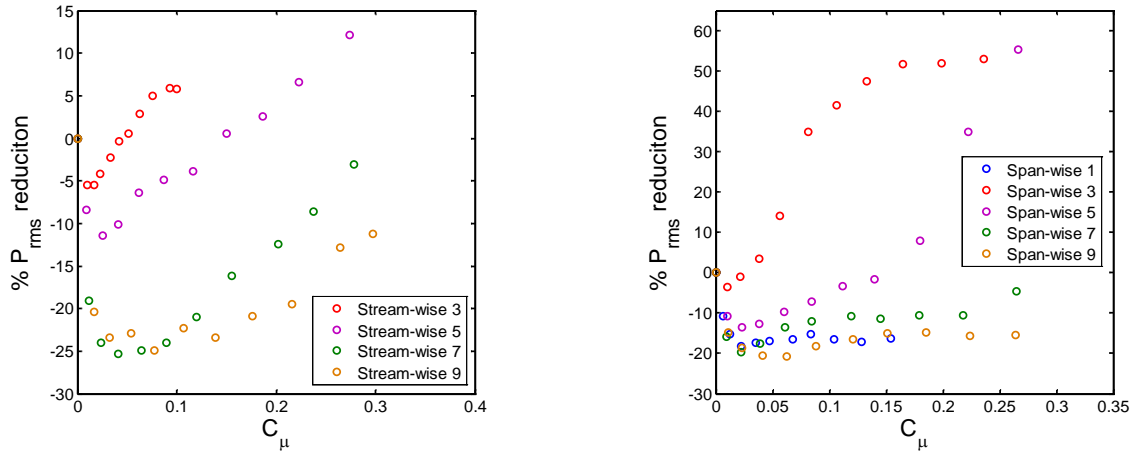


Figure 22: Mach 0.6, fluctuating surface pressure reduction at the aft wall.

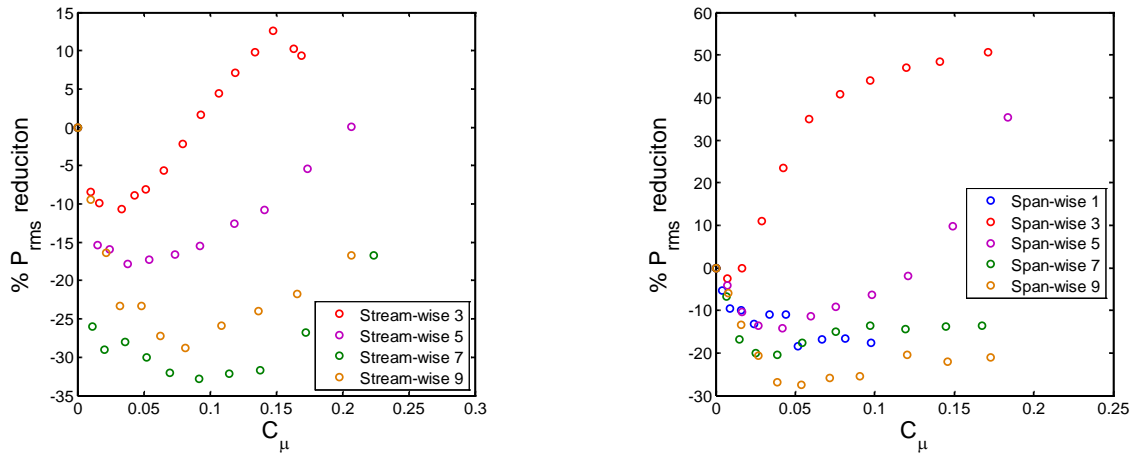


Figure 23: Mach 0.7, fluctuating surface pressure reduction at the aft wall.

Figure 24 shows typical instantaneous Schlieren images which indicate representative flow fields for Mach 0.5 to 0.7 for the acoustically-treated tunnel ceiling. The flow direction is from left to right. The vortical flow structures are clearly observed in the figure. The region where the shear layer structures interact with the trailing edge of the cavity is also clearly seen as a region of intense fluctuations in the density gradient field. When the control is on, the mass injection may modify the vortical structure which impinges onto the trailing edge of the cavity. The reduction in both the shear layer fluctuations and the radiated acoustic field are observed.

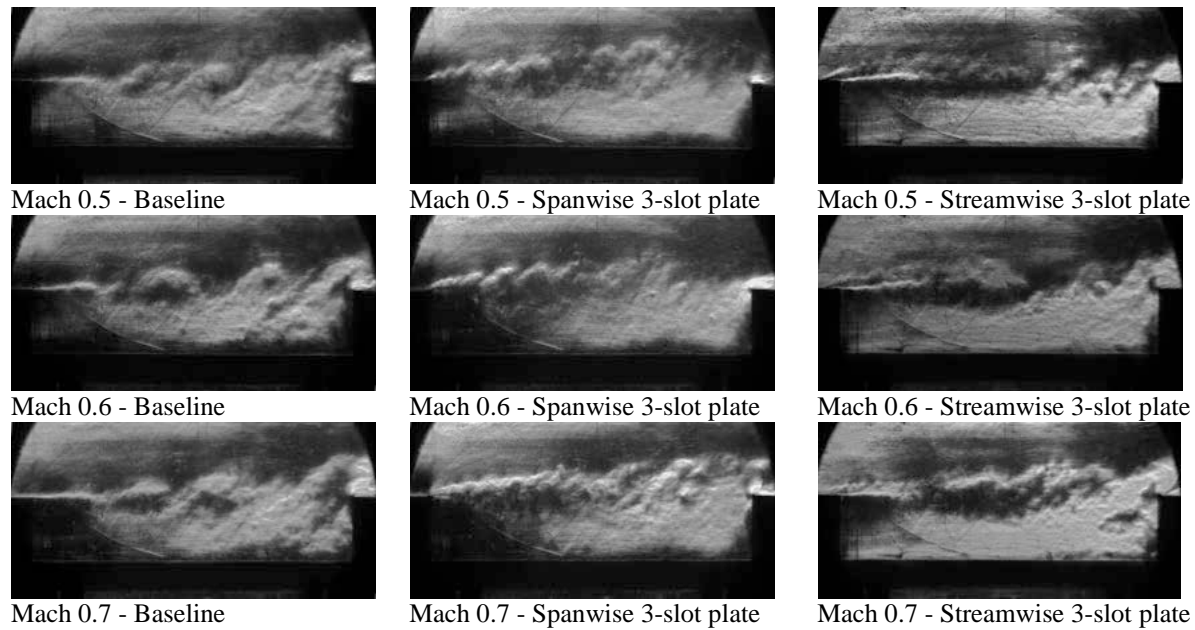


Figure 24: Instantaneous Schlieren photographs of flow over the cavity. Flow direction is from left to right.

2.2.3 Summary

The results of a study with steady blowing at the cavities leading edge in subsonic free stream conditions yielded similar results to previous work performed with a supersonic free stream conditions. Mass injection through the leading edge slot was shown to suppress the combined peak and broadband components of the fluctuating surface pressure by as much as 50%. In comparing the orientation of the slots, it was shown that spanwise aligned slots needed lower mass flow rates to approach higher reductions in the fluctuating surface pressure than streamwise aligned slots. The spanwise aligned 3-slot plate demonstrated the most effective performance over the range of conditions investigated here. The Schlieren images presented above show that the flow structure appears to be more dominated by small scales structures for the cases where the leading edge blowing resulted in reductions of the fluctuating surface pressure.

3 Adaptive Control using Time Dependent Leading Edge Excitation

One of the objectives of this research is to develop adaptive control methodologies that can be used for any flow condition to reduce the surface pressure fluctuations in open cavities. The following section will discuss the application of several different adaptive control algorithms that were applied using time dependent actuation at the cavities leading edge. The discussion will be broken up into four sections. First, the control algorithms will be presented. This is followed by a discussion of the actuators and a presentation of the results. Finally, a summary will be presented.

3.1 Control Algorithms

This section outlines the three closed-loop control algorithms used to compare to open-loop control in this study. The algorithms include downhill simplex, ARMARKOV adaptive disturbance rejection, and GPC. For each of these applications, the control goal is to minimize the fluctuating surface pressure of the cavity using ZNMF actuators at the leading edge of the cavity.

3.1.1 Downhill Simplex Algorithm

The DS method (Nelder and Mead, 1965) is a minimization process that is capable of optimizing N -dimensional systems. It minimizes an objective function and is similar to extremum seeking (see Maury et al., 2009 and the references therein) in that a time-averaged extremum of the cost function is assumed to exist. For an open cavity flow, the objective function is the integrated pressure fluctuation near the trailing edge of the cavity over a prescribed frequency range (i.e., 100 Hz – 4.0 kHz in this study). The algorithm aims to minimize the objective function by changing the relevant waveform parameters of the actuators input such as amplitude and frequency.

The downhill simplex algorithm is a simple method and is attractive in experiments since it only requires evaluation of the cost function and not its derivatives (Press et al., 1992). To understand the algorithm, we first define a simplex as a geometrical structure which consists of $N + 1$ vertices (in N dimensions). For instance, a simplex in two dimensions is a triangle. The downhill simplex algorithm makes use of the geometrical concept of a simplex and searches downhill in a straightforward fashion that makes no prior assumptions about the function. It can thus potentially be slow. However, it is guaranteed to find a local minimum (Press et al., 1992), as shown in Figure 25. The algorithm modifies the simplex repeatedly according to following procedure:

Given initial values of a simplex of $N+1$ vertices for N -dimensional vector \bar{x} , which contains the parameters to be optimized, order the points so that

$$f(\bar{x}_{n+1}) > f(\bar{x}_n) > \dots > f(\bar{x}_2) > f(\bar{x}_1). \quad \text{Eq. 4}$$

Reflect the vertex associated with the largest function evaluation about the simplex centroid to generate a reflected trial point \bar{x}_r ,

$$\bar{x}_r = \bar{x}_{cen} + m(\bar{x}_{cen} - \bar{x}_{n+1}) \quad \text{Eq. 5}$$

where $\bar{x}_{cen} = \sum_i^{N+1} \bar{x}_i / (N+1)$ is the centroid and $m > 0$.

Compute $f(\bar{x}_r)$.

If

$$f(\bar{x}_r) < f(\bar{x}_1), \quad \text{Eq. 6}$$

i.e., \bar{x}_r is the new optimum, then the assumed direction of reflection is correct, so expand the search in this direction.

$$\bar{x}_e = \bar{x}_r + \alpha(\bar{x}_r - \bar{x}_{cen}), \quad \text{Eq. 7}$$

where $\alpha > 0$. If $f(\bar{x}_e) < f(\bar{x}_r)$, then replace \bar{x}_{n+1} by \bar{x}_e , otherwise, the expansion fails, so replace \bar{x}_{n+1} by \bar{x}_r . Else, proceed to step 3b.

If

$$f(\bar{x}_r) > f(\bar{x}_1), \quad \text{Eq. 8}$$

the reflection fails. So generate a new point by contraction

$$\bar{x}_c = \bar{x}_{cen} + \beta(\bar{x}_{n+1} - \bar{x}_{cen}), \quad \text{Eq. 9}$$

where $0 < \beta < 1$. If $f(\bar{x}_c) < f(\bar{x}_{n+1})$, then replace \bar{x}_{n+1} by \bar{x}_c , otherwise contract again.

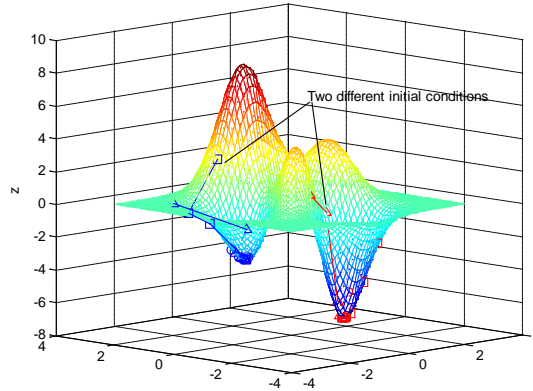


Figure 25: Illustration of downhill simplex algorithm for two-dimensional objective function Z with two different initial conditions.

3.1.2 ARMARKOV Adaptive Disturbance Rejection Algorithm

The ARMARKOV disturbance rejection algorithm was introduced in Venugopal and Bernstein (1997) and had been used by Cattafesta et al. (1999) for control of cavity oscillations and Tian et al. (2006) for control of flow separation. The algorithm uses a linear model that is identified simultaneously using the recursive ARMARKOV/Toeplitz system identification algorithm. Readers are referred to Venugopal and Bernstein (1997) for details of the derivation of the algorithm.

Figure 26 shows a block diagram of a standard disturbance rejection problem, where w is the unknown disturbance input, u is the control signal, y is the reference signal, z is the performance signal, and G_c is the disturbance rejection controller. In addition, for the four transfer matrices, G_{zw} is the primary path, G_{zu} is the secondary path, G_{yw} is the reference path, and G_{yu} is the feedback path. The secondary path G_{zu} is required to be identified by online or offline system identification methods. Figure 27 shows the block diagram of the application of the ARMARKOV disturbance rejection algorithm to control cavity oscillations, where system identification uses either band-limited white noise or a periodic chirp signal as the input to the actuator. The signals z and y can be measured using unsteady pressure sensors, which are presumed to be linear combinations of an unknown disturbance w and an actuator control input u . The signal y is used for feedback, while the signal z is used for performance evaluation. In this study, both signals are measured by an unsteady pressure sensor which is located near the trailing edge. It is assumed that the actuator signal u is a linear combination of past actuator inputs and current and past measured unsteady pressure sensor outputs. The goal of the adaptive controller is thus to select optimal weights to minimize the power of the fluctuating pressure. The weights should change slowly compared to the fluid dynamic time scales, so the cost function with respect to the weights is minimized to obtain the adaptive control law. The weights are adjusted in an iterative fashion in real time using a gradient descent algorithm. The controller requires the following parameters as inputs: the order of the system n , the number of Markov parameters for system identification μ , the order of the controller n_c , the number of controller Markov parameters μ_c , the parameter p that controls the memory of the controller to past events, and the sampling rate. Increasing parameters (n , μ , etc.) may improve performance but will significantly increase the computational costs (Cattafesta et al., 1999). Moreover, the sampling rate and other parameters (n , μ , etc.) must be tuned to acquire a balance between temporal resolution and performance.

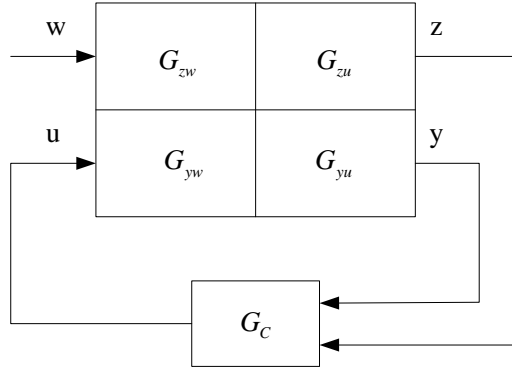


Figure 26: Block diagram for two-input, two-output disturbance rejection control.

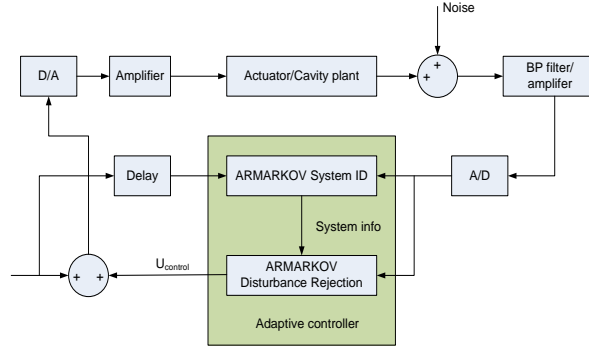


Figure 27: Block diagram of ARMARKOV.

3.1.3 Generalized Predictive Control Algorithm

The GPC algorithm was introduced in Clarke et al. (1987). The GPC algorithm is based on system output predictions over a finite time horizon. An appropriate cost function is then defined using these predictions and minimized to determine the control law. The GPC algorithm has been applied to active vibration and noise control. Kegerise et al. (2007) also demonstrated the potential for this control approach to suppress cavity oscillations.

Briefly, to develop an adaptive GPC algorithm, a predictive matrix equation that provides future system output predictions is formed:

$$\mathbf{y}_s(k) = \mathbf{T}\mathbf{u}_s(k) + \mathbf{B}\mathbf{u}_p(k-p) + \mathbf{A}\mathbf{y}_p(k-p) \quad \text{Eq. 10}$$

where $\mathbf{y}_s(k)$ is a vector of current and future outputs (superscript T below denotes transpose):

$$\mathbf{y}_s(k) = (y(k) \quad y(k+1) \quad \cdots \quad y(k+s-1))^T \quad \text{Eq. 11}$$

$\mathbf{u}_s(k)$ is a vector of current and future inputs:

$$\mathbf{u}_s(k) = (u(k) \quad u(k+1) \quad \cdots \quad u(k+s-1))^T \quad \text{Eq. 12}$$

$\mathbf{y}_p(k-p)$ is a vector of past outputs running from time step from $k-p$ to $k-1$:

$$\mathbf{y}_p(k-p) = (y(k-p) \quad y(k-p+1) \quad \cdots \quad y(k-1))^T \quad \text{Eq. 13}$$

and $\mathbf{u}_p(k-p)$ is a vector of past inputs running from time step from $k-p$ to $k-1$:

$$\mathbf{u}_p(k-p) = (u(k-p) \quad u(k-p+1) \quad \cdots \quad u(k-1))^T \quad \text{Eq. 14}$$

Eq.10 shows that the current and future outputs (with a prediction horizon s) are a linear combination of the current and future inputs and past input/outputs. The parameter matrices (\mathbf{T} , \mathbf{B} and \mathbf{A}) in the equation are determined through system identification in a time-dependent fashion.

To reject the disturbance at the system output, an appropriate scalar cost function for the GPC algorithm is given by:

$$J(k) = \frac{1}{2} \left(\mathbf{y}_s^T(k) \mathbf{Q} \mathbf{y}_s(k) + \mathbf{u}_s^T(k) \mathbf{R} \mathbf{u}_s(k) \right) \quad \text{Eq. 15}$$

The first term in the cost function is a weighted sum of the squares of current and future outputs. The second term acts as a penalty on the control effort. This term is necessary to avoid large control inputs and actuator saturation. To determine the control law, the cost function is minimized with respect to the control input. Substituting Eq. 10 into Eq. 15 and minimizing the result with respect to $\mathbf{u}_s(k)$ leads to:

$$\mathbf{u}_s|_{opt} = [\mathbf{H}] \begin{bmatrix} \mathbf{u}_p(k-p)^T & \mathbf{y}_p(k-p)^T \end{bmatrix}^T \quad \text{Eq. 16}$$

Where:

$$[\mathbf{H}] = -(\mathbf{T}^T \mathbf{Q} \mathbf{T} + \mathbf{R})^{-1} \mathbf{T}^T \mathbf{Q} [\mathbf{B} \quad \mathbf{A}] \quad \text{Eq. 17}$$

The matrix of controller coefficients \mathbf{H} minimizes the cost function. A computationally efficient way to compute \mathbf{H} is to use a gradient-descent algorithm:

$$\mathbf{H}(k+1) = \mathbf{H}(k) - \mu \frac{\partial J(k)}{\partial \mathbf{H}(k)} \quad \text{Eq. 18}$$

Here, the controller coefficients are updated at each time step (since \mathbf{T} , \mathbf{B} and \mathbf{A} vary with time) using the previous set of coefficients and a stochastic estimate of the cost-function gradient, which can be computed using input/output data and the identified process parameters. Similar to the ARMARKOV method, the cost function is the power of the fluctuating pressure signal at the trailing edge of the cavity. If the model order is low enough or if the identified parameters are assumed constant, the matrix inverse can be computed and \mathbf{H} is found using Eq. 17. In practice, only the current input $u(k)$ is used in Eq. 12.

Several parameters in the GPC algorithm must be tuned to achieve a trade-off between the control performance and stability: the model order p , the prediction horizon s , the control effort penalty \mathbf{R} , the sensor weights \mathbf{Q} , and the sample rate. The model order p and the prediction horizon s are selected through the system identification. The model order p should be large enough in order to adequately model the relevant open-loop dynamics.

3.2 Actuators

The piezoelectric ZNMF synthetic jet actuator array mounted at the leading edge of the cavity consists of five identical cells as shown in Figure 28. Details of the actuator design are provided in Arunajatesan et al. (2009). Each cell contains a commercially available parallel operation bimorph piezoelectric disc (APC 850 from APC Inc.) separating two cavities with slightly different volumes. The advantage of such a design is that it avoids the dc pressure imbalance on the two sides of the diaphragm during the experiment. Three slot geometries for the synthetic jet are investigated for their control performance considering the jet output velocity and interactions with the boundary layer on the leading edge. Each geometry is tabulated in the Table 6.

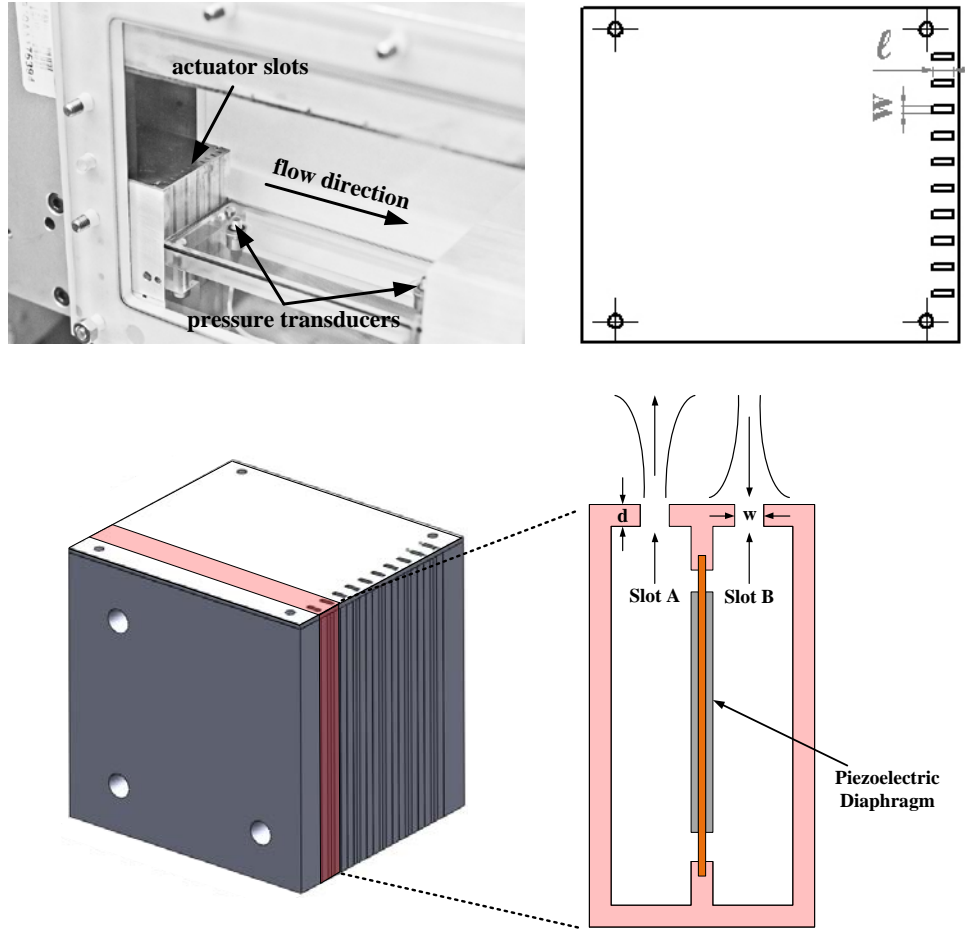


Figure 28: Actuator array block. The topmost figure illustrates the actuator array installed in the wind tunnel as well as the top plate. The bottommost figure illustrates the entire actuator array as well as one of the single cells that comprise the actuator array.

Table 5: Geometry of each slot in the top plates (Units: mm).

	Plate 1 (Reference plate)	Plate 2 (High aspect ratio)	Plate 3 (Smallest slot area)
Length (l)	3.0	3.0	1.5
Width (w)	1.0	0.5	0.5
Depth (d)	1.0	1.0	1.0

In order to implement the open-loop control, a signal with specified waveform parameters is generated by an Agilent 33220A Function/Arbitrary Waveform Generator and is used to excite the actuator array through a Trek PZD350 Piezo Driver/Amplifier. In addition to sinusoidal excitation, amplitude modulation and burst modulation excitation waveforms (Takahashi et al., 2011) are also used. Each input waveform is described as follows:

(a) Sinusoidal

$$V(t) = A \sin(\omega_c t) \quad \text{Eq. 19}$$

(b) AM

$$V(t) = A \sin(\omega_c t) \sin(\omega_m t) \quad \text{Eq. 20}$$

(c) BM

$$V(t) = A \sin(\omega_c t) \text{Mod}(\omega_m) \quad \text{Eq. 21}$$

where the amplitude A has unit of volts, and the carrier frequency f_c ($= \omega_c/2\pi$) and modulation frequency f_m are in Hz. The “Mod” function is either a sinusoid or square pulse.

In order to implement the downhill simplex control, the rms trailing edge pressure fluctuation integrated over a prescribed frequency range (i.e., 100 Hz – 4.0 kHz in this study) is normalized by the free stream dynamic pressure and is used as the objective function. The control algorithm aims to minimize the objective function by changing the relevant waveform parameters: amplitude A , carrier frequency f_c , and modulation frequency f_m .

For the ARMARKOV adaptive disturbance rejection control and generalized predictive control (GPC), the signal from the trailing edge transducer is pre-amplified and low-pass filtered using a Kemo multi-channel filter (Model VBF 35). The cutoff frequency is set to be 4 kHz for a sampling frequency of 10.24 kHz. This signal is then sampled with a 5-channel, 16-bit simultaneous sampling dSPACE ADC (model DS2001). The control algorithms are coded in SIMULINK s-functions and are compiled via Matlab/Real-time workshop (RTW). These codes are then uploaded and run on the dSPACE digital control system, which collects inputs/outputs from DS2001ADC boards and computes the control signal once per time step. The output signal from dSPACE is passed through Kemo filter to smooth the zero-order hold signal from the DAC. The signal from this filter is then fed through the Trek amplifiers to drive the actuator array.

A z-type mirror based Schlieren system was used for flow visualization. Details are described in Takahashi et al. (2011). The light source is a strobe light (Perkin Elmer Inc.). The beam diameter of the light from the beam expander, which is neighboring the light source, is 25 mm. A f4/100 mm condenser lens focuses the light on an adjustable rectangular aperture. This aperture is placed at the focal point of the first parabolic mirror. Two parabolic mirrors of 152.4 mm diameter with focal length of 609.6 mm and 1524 mm are used to produce a parallel beam passing through the test section. A second parabolic mirror focuses the light on the knife-edge position. The knife-edge direction is horizontal so as to visualize the transverse density gradient of the flow. In order to reduce the light intensity entering the camera, a neutral density filter is attached in front of the camera lens. The Schlieren image is captured by a CCD camera (Powerview plus 2M, TSI Inc.) through a Nikon AF Micro 60mm f/2.8D lens.

3.3 Actuator Characterization

The measured velocity output for three peak-to-peak voltage (V_{p-p}) inputs of the actuator are shown in Figure 29, where the centerline velocity (amplitude) of the third cell (in the middle of the actuator array) for the slot plate 1 is presented. Due to the differing cavity size on either side of the piezoelectric bimorph, the jet velocity for each slot in a pair differs. The result

demonstrates broadband output and a peak velocity greater than 100 m/s near 1100 Hz in the faster slot. Figure 30 compares the centerline velocity and momentum coefficient at the slot in the slow slot of the third cell for the three slot plates listed in Table 6. The momentum coefficient is calculated by assuming incompressible flow and normalized by the momentum flux in the boundary layer which spans the leading edge: $1/2 \rho_{\infty} U_{\infty}^2 W_c \delta$, where ρ_{∞} is the density of free stream, U_{∞} is the free stream velocity, W_c is cavity width, and $\delta=2.96$ mm is the measured boundary layer thickness at the leading edge of the cavity for Mach 0.3. Each plate has a similar trend of increasing velocity with input voltage and has a similar shape in the frequency response with the maximum velocity occurring near 1100 Hz for each plate. The high aspect ratio slot, plate 2, shows the highest output velocity, while the smallest slot area, plate 3, shows higher output velocity than slot plate 1. However the reference slot, plate 1, generates the highest output of momentum, while the smallest slot, plate 3 produces much less momentum.

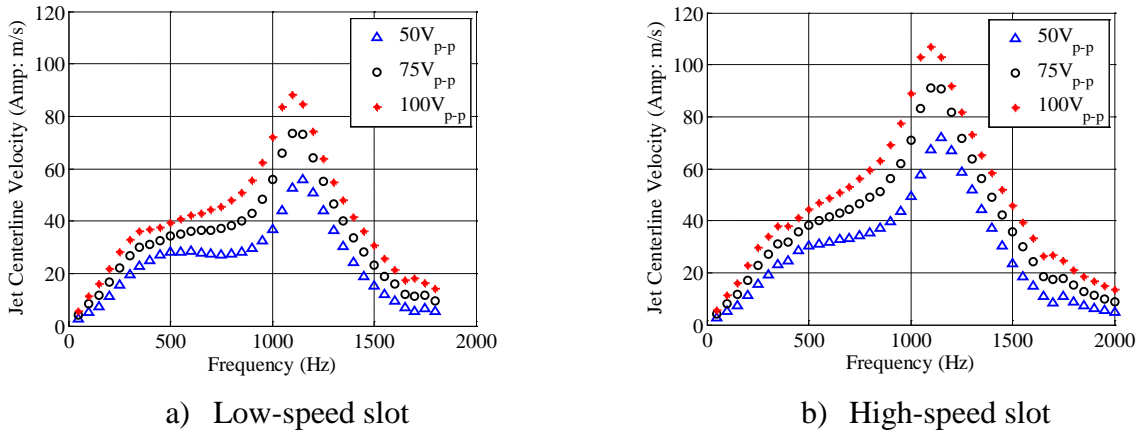


Figure 29: Centerline velocity of the third cell of the slot plate 1 actuator array.

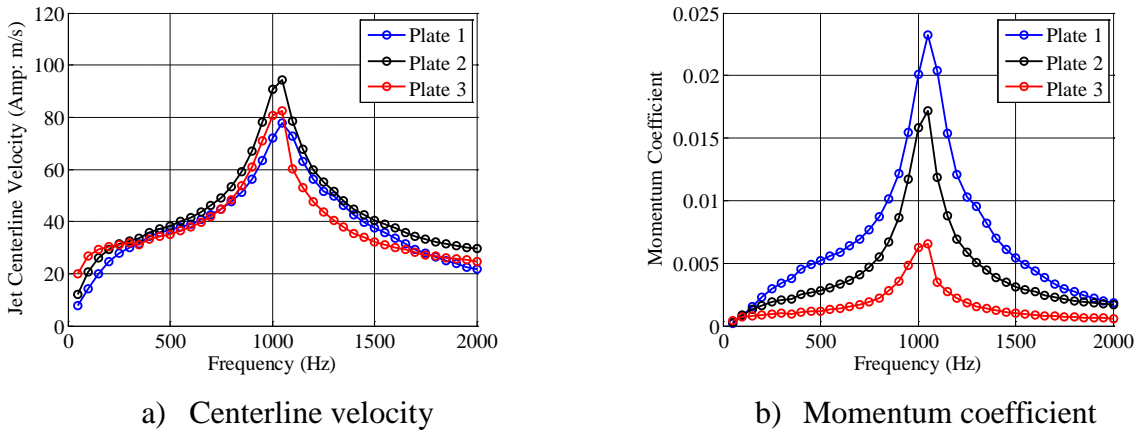


Figure 30: Comparison of centerline velocity and momentum coefficient in the low-speed slot for three slot plates (input voltage: 75 V_{p-p}).

3.4 Flow Control Results

Figure 31 shows the probability density function for Rossiter mode 2 in the baseline trailing edge pressure signal at $M = 0.3$. For the plot, the fluctuating pressure measurements are band-pass filtered around each Rossiter mode using a KEMO VBF-35 analog filter. In each case, the band-pass frequencies are set to ± 10 Hz of the Rossiter mode frequency. The values of mean, standard deviation (STD), skewness, and kurtosis for Rossiter mode 2 are summarized in Table 7, as well as the results for modes 3 to 5. The results show that the probability density functions for mode 2 and the other modes, which are not shown here, are nearly Gaussian. As described in Rowley et al., (2006) this is an indication of a lightly damped, linearly stable system that is constantly excited by external disturbances in the upstream boundary layer. These disturbances are amplified, causing oscillations at the resonant frequencies of the cavity. If the disturbances are removed, however, the oscillations would no longer be present. This implies the cavity oscillations may therefore be characterized as a forced, linearly stable system. Therefore, the use of system identification to the open-loop system, and adaptive feedback control algorithms (e.g., GPC and ARMARKOV) is justified for use to suppress the cavity oscillations in this study.

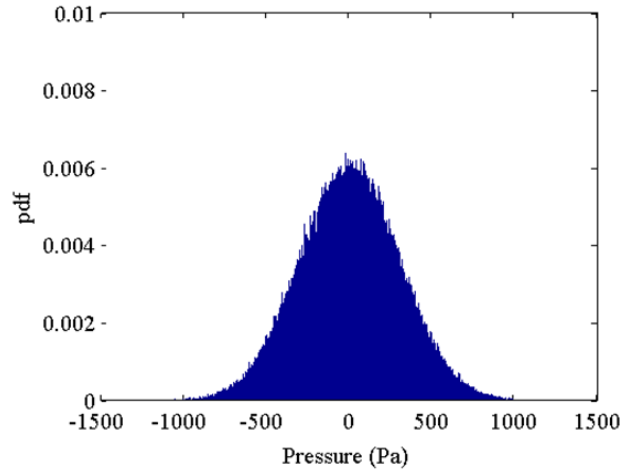


Figure 31: Probability density function for Rossiter mode 2 (880 Hz) in the trailing edge baseline at $M=0.3$.

Table 6: Statistics of each Rossiter mode in Figure 31.

	Mean (Pa)	STD (Pa)	Skewness	Kurtosis
Mode 2 (880 Hz)	0.00	271	0.01	3.04
Mode 3 (1280 Hz)	0.00	242	0.01	3.04
Mode 4 (1820 Hz)	0.00	241	0.00	3.04
Mode 5 (2320 Hz)	0.00	232	0.00	3.03

Figure 32 shows the results for the OL sinusoidal control at Mach 0.3 and 0.4. In particular, spectra of the trailing edge fluctuating surface pressure (P_{rms}) normalized by the averaged free stream dynamic pressure (Q) are presented. The peaks seen in the figures for the baseline uncontrolled cases are due to the well-known Rossiter modes. Note that the sharp peaks at 1100 Hz and 2200 Hz for the controlled cases are associated with the acoustic signal produced

by the actuator array. For all OL sinusoidal control cases, maximum suppression corresponds to forcing at 1100 Hz. This is presumably because this frequency is close to the resonant frequency of the actuator but sufficiently removed from a cavity resonance frequency to initiate lock-on resonance to the forcing frequency. While broadband suppression is achieved at $M=0.4$, tonal suppression is reduced, indicating a larger jet velocity is required for control. The reduction of overall power and percent reduction of trailing edge pressure fluctuation for both Mach number cases are tabulated in Table 8. Higher input voltages, which produce larger output jet velocities as seen in Figure 29, show better control performance up to a point. These results suggest the existence of either an optimal value (at Mach 0.3) or saturation (at Mach 0.4) of the voltage amplitude for the range of input voltages considered. Note that sufficiently high input voltage ultimately leads to failure of the piezoceramic discs.

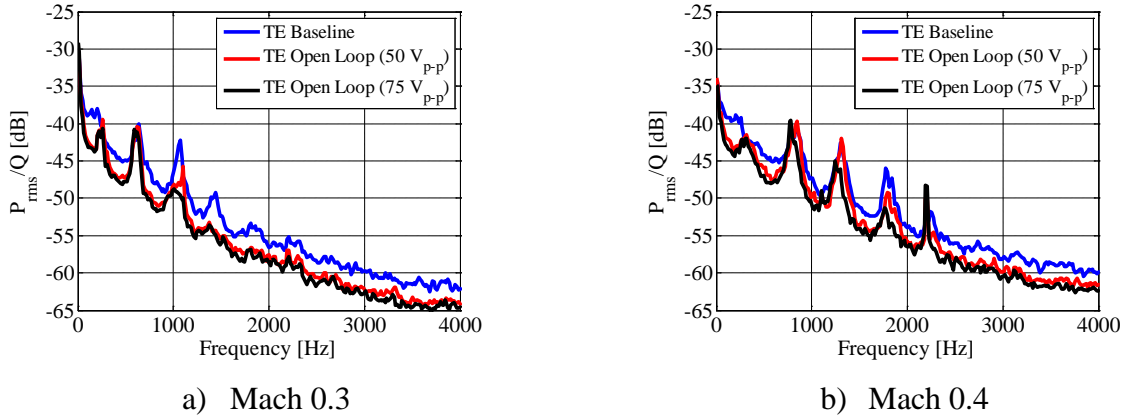


Figure 32: OL sinusoidal control results, where $f = 1100$ Hz and $V_{p-p} = 50$ V or 75 V.

Table 7: Comparison of control performance against the input voltage for Mach 0.3 and 0.4.

Input Voltage [V_{p-p}]	Mach 0.3		Mach 0.4	
	Overall power reduction [dB]	% reduction in rms pressure fluctuations	Overall power reduction [dB]	% reduction in rms pressure fluctuations
50	-2.5	24.7	-1.6	16.7
75	-3.2	30.4	-2.4	24.4
100	-1.9	19.6	-2.5	24.7

Figure 33 compares the percent reduction of trailing edge pressure fluctuation (P_{rms}) for three different slot geometries in the OL sinusoidal control for Mach 0.3 and 0.4, respectively, for an input voltage is $75 V_{p-p}$. The reduction in P_{rms} between the baseline and OL sinusoidal case is largest at 1100 Hz and shows the best performance from 1000 Hz to 1200 Hz. These results coincide with the actuator output at resonance, indicated by the centerline jet velocity of the synthetic jet in Figure 30. Plate 1 performs best (particularly at Mach 0.4). From the results in Figure 30, plate 1 provided the smallest actuator output velocity but the highest momentum of all plate configurations. The higher momentum alters the shear-layer near the leading edge and consequently influences the flow-induced resonance. However, there are several parameters that

may contribute to the control effectiveness. Other relevant parameters beyond the velocity ratio and momentum coefficient include the slot aspect ratio. These preliminary results suggest a more detailed analysis and study of these parameters are warranted.

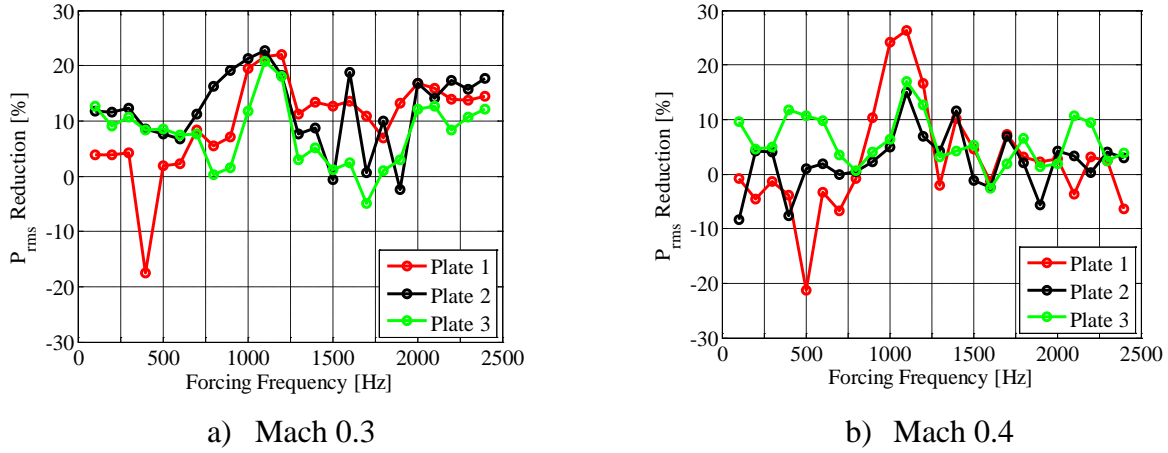


Figure 33: Comparison of P_{rms} reduction [%] for three different slot geometries in open-loop sinusoidal control. The input voltage is $75V_{p-p}$, and frequency is swept from 100 Hz to 2400 Hz in steps of 100 Hz.

Figure 34 through Figure 36 show the results of downhill simplex control at Mach 0.3. For three waveform types (sinusoidal, AM and BM), the DS algorithm arrives at nearly the same carrier forcing frequency as the OL case but in a small fraction of the time. It should be noted that the DS simplex generally finds a local minimum, and hence the optimized results depend on the initial conditions and constraints. In this case, the forcing frequency is constrained between 500 Hz and 1500 Hz, and this range is chosen to include the resonance frequency of the actuator. The results indicate again that both tones and broadband noise level are mitigated using these schemes. Multiple Rossiter modes are reduced but are not eliminated, and the second Rossiter mode remains the strongest. The broadband pressure fluctuations are reduced over the entire frequency range of interest (~ 4 kHz). The reason for this reduction may be due to the mean-flow modification provided by the three-dimensional perturbations introduced by the actuator. By comparison, approximately 2.5 dB versus 2.6 dB in overall power reduction which corresponds to 24.7% versus 26.0% reduction of the pressure fluctuation are obtained for the OL and DS sinusoidal cases, respectively. In addition, continuous sinusoidal forcing is better than either the AM or BM case.

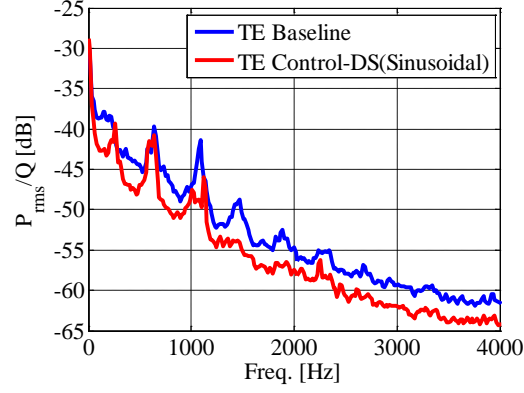


Figure 34: Downhill simplex (sinusoidal) control results, Mach = 0.3, $f_c = 1125$ Hz and $V_{p-p} = 50$ V.

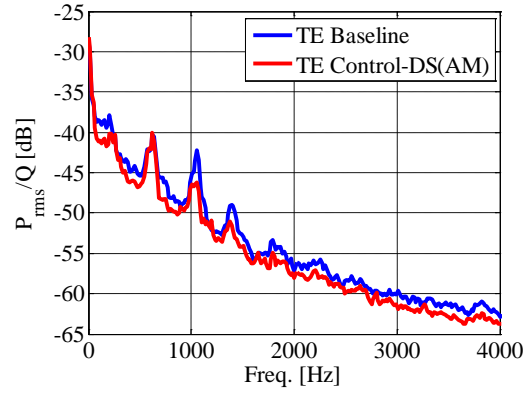


Figure 35: Downhill simplex (amplitude modulation) control results, Mach = 0.3, $f_m = 42$ Hz, $f_c = 1200$ Hz, and $V_{p-p} = 50$ V

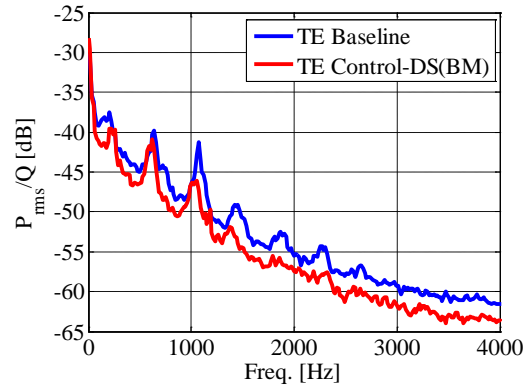


Figure 36: Downhill simplex (burst modulation) control, Mach = 0.3, $f_m = 40$ Hz, $f_c = 1180$ Hz, and $V_{p-p} = 50$ V.

Figure 37 and Figure 38 show preliminary ARMARKOV and GPC control results, respectively. The ARMARKOV and GPC algorithms are somewhat less effective compared to the OL and DS, presumably due to the reduced coherence (not shown) between the input and output signals. The three-dimensional forcing disrupts the spanwise coherence of the shear-layer perturbations, and this disruption reduces the coherence between the control input and pressure output signals. The reduced coherence leads to poorer dynamical models and reduced control performance relative to two-dimensional slot forcing along the entire leading edge (Kegerise, et al., 2007). The reduction in overall sound pressure level (OASPL) and rms pressure fluctuations for all control methods at Mach 0.3 are summarized in Table 9. Comparisons show that non-model based simplex algorithms have demonstrated their efficacy to reduce both the tonal and broadband components for the given test condition. Results for Mach 0.4 cases are summarized in Table 4 as well. Due to the reduced control performance for Mach 0.4 case at 50 V_{p-p} , the results are obtained with 75 V_{p-p} .

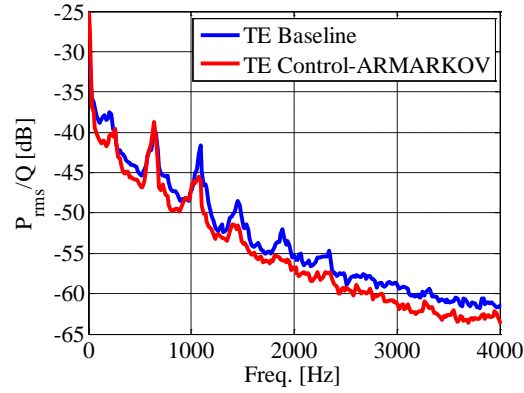


Figure 37: ARMARKOV control results, Mach = 0.3, model order $n = 6$ and Markov parameter number $\mu = 10$.

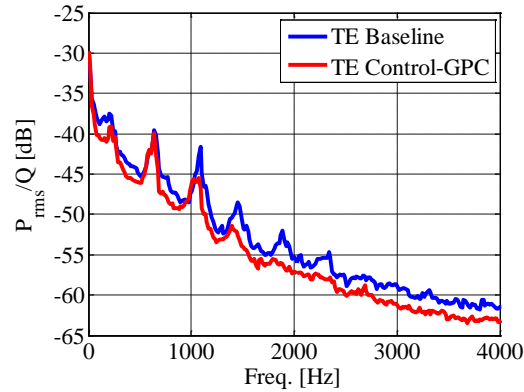


Figure 38: GPC control, Mach = 0.3, model order $p = 20$, and horizon $s = 6$.

Table 8: Summary of performance of different control methods for Mach 0.3 and 0.4 flows.

Control Method	Mach 0.3 (50 V _{p-p})		Mach 0.4 (75 V _{p-p})	
	Overall power reduction [dB]	% reduction in rms pressure fluctuations	Overall power reduction [dB]	% reduction in rms pressure fluctuations
Open-Loop	-2.5	24.7	-2.4	24.4
DS – Sinusoid	-2.6	26.0	-3.1	30.3
DS – AM	-1.3	13.9	-1.1	11.5
DS – BM	-1.9	19.5	-2.2	22.4
ARMAKOV	-1.6	16.8	-	-
GPC	-1.6	16.7	-	-

3.5 Summary

The results of a comparative study aimed at efficient active suppression of flow-induced cavity oscillations are presented. Through the investigation of different actuator slot geometries, larger slots which generate larger momentum with a forcing frequency near the resonant frequency of the actuator showed the best performance for suppressing the cavity oscillation. Up to 30% reduction in the rms pressure fluctuations in a 4 kHz bandwidth are obtained using various open-loop and closed-loop controllers via a zero-net mass-flux actuator array at the cavity leading edge. In addition, multiple Rossiter-mode noise reduction was also demonstrated. Kegerise et al. (2007) previously demonstrated multiple Rossiter mode suppression using active control, but broadband noise suppression was not possible in their study because of the two-dimensional nature of the perturbation inputs. Brès and Colonius (2008) showed that three-dimensional spanwise control, in which each actuator has a different phase angle, was potentially more effective than two-dimensional control. Therefore as a next step, a flow visualization study to understand the effects of OL and CL control on the flow physics in order to develop an effective but efficient control scheme is necessary. Hence, future work will focus on acquisition of quantitative Schlieren (Background Oriented Schlieren: BOS) and particle image velocimetry (PIV) measurements obtained simultaneously with unsteady surface pressure measurements. These data will help determine the relationships between pressure, velocity, and density and consequently help to develop better control methodologies.

4 Project Summary and Future Work

In this project we have studied various aspects of applying active control to high speed flow over open cavities. Key aspects of this study involved the acquisition and analysis of supersonic flow field data of a successfully controlled open cavity flow and the application of closed loop adaptive control methodologies. Summaries have been provided above for each phase of the study, however listed below is a few of the key findings.

- Surface pressure measurements for both supersonic and subsonic free stream conditions have demonstrated the advantage of introducing control with spanwise perturbations highlighting the need for three dimensionality in the control scheme.
- The segmented slot blowing at the cavities leading edge allowed for the creation of streamwise aligned vortical structures which allowed for transport of momentum between the cavity and free stream altering how the cavity shear layer interacted with the aft wall.
- Segmented slots where the major axis was perpendicular to the oncoming flow were more effective at reducing the fluctuating surface pressure, most likely due to size and strength of the streamwise aligned vortical structures created.
- Successful application of adaptive flow control has been demonstrated that reduced multiple tonal components as well as the broad band levels.

This study has led to a better understanding of many aspects of high speed flows over open cavities however there are many avenues for future work which may include;

- the use of global stability analysis determine spanwise wavelengths and frequencies for more efficient control.
- the development of time dependent actuation that has the authority to be used in supersonic free stream conditions.
- the extension of the work to the transonic regime as that represents important realistic flight conditions where active control of cavity flows could be applied.
- the development of model based adaptive control algorithms to improve our ability to couple the flow control with the flow physics.

5 Publications and Students Supported

5.1 Students/Post Docs

- George Shumway (Partial Support - M.S., Dec. 2009)
- Taylor Lusk (M.S. May 2011)
- Kyle Hughes (PhD expected May 2015)
- Hidemi Takahashi (Post-Doctoral Scientist)
- Yang Zhang (PhD expected May 2015)

5.2 Publications/Presentations

- Journals
 - Lusk, T., Cattafesta, L., and Ukeiley, L., “Leading Edge Slot Blowing on an Open Cavity in Supersonic Flow,” (2012) *Experiments in Fluids*, Vol. 53, No. 1, pp. 187-199.
 - Takahashi, H., Liu, F., Palaviccini, M., Oyarzun, M., Griffin, J., Ukeiley, L. and Cattafesta, L., “Experimental Study of Adaptive Control of High-Speed Flow-Induced Cavity Oscillations,” (2011) *Journal of Fluid Science and Technology*, Vol. 5, No. 5, pp. 701-716.
- Conference
 - Takahashi, H., Liu, F., Palaviccini, M., Oyarzun, M., Griffin, J., Ukeiley, L., and Cattafesta, L., "Progress on Active Control of Open Cavities", *49th AIAA Aerospace Sciences Meeting including the New Horizons Forum and Aerospace Exposition*, AIAA 2011-1221, Orlando, FL, AIAA, 01/2011.
 - Lusk, T., Dudley, J., Ukeiley, L., and Cattafesta, L., (2011) “Flow Field Effects of Control on Supersonic Open Cavities,” AIAA Paper 2011-0039, AIAA Aerospace Sciences Meeting
 - Takahashi, H., Liu, F., Palaviccini, M., Oyarzun, M., Ukeiley, L., and Cattafesta, L., "Experimental Study of Adaptive Control of High-Speed Flow-Induced Cavity Oscillations", *Seventh International Conference on Flow Dynamics*, Sendai, Japan, Tohoku University Global COE Program , 11/2010.
- Presentations
 - “Flow over Open Cavities and Their Control,” Clarkson University, November, 2011.
 - Ukeiley, L., “Open Loop Control of Supersonic Cavity Flows,” Air Force Research Laboratory Vehicles Directorate, Wright-Patterson Air Force Base, Dayton, OH, May 2011.
 - “Flow over Open Cavities and Their Control,” University of Florida, September, 2010.

- Ukeiley, L., and Cattafesta, L., “Active Control of Open Cavities,” Minnowbrook VI: Flow Physics and Control for Internal and External Aerodynamics, August 2009.

6 List of References

- Arunajatesan, S., Kannepalli, C., Sinha, N., Shumway, G., Ukeiley, L., Sheehan, M. and Alvi, F., "Suppression of Cavity Loads Using Leading Edge Blowing Concepts," AIAA Journal, 2009.
- Arunajatesan, S., Oyarzun, M., Palavicchini, M., and Cattafesta, L., Modeling of Zero-Net Mass-Flux Actuators for Feedback Flow Control, 47th AIAA Aerospace Sciences Meeting, AIAA Paper 2009-0743, 2009.
- Bendat, J. S., and Piersol, A. G., Random Data: Analysis & Measurement Procedures, John Wiley & Sons, Inc., New York, NY, 2000.
- Brès, G. A., and Colonius, T., "Three-Dimensional Instabilities in Compressible Flow Over Open Cavities," *Journal of Fluid Mechanics*, Vol. 599, pp. 309-339.
- Brown, G. L., & Roshko, A. (1974). On density effects and large structure in turbulent mixing layers. *Journal of Fluid Mechanics*, 64, 775-816, 2008.
- Bueno, P. C., Ünalms, Ö., H., Clemens, N. T., and Dolling, D. S., "The Effects of Upstream Mass Injection on a Mach 2 Cavity Flow," AIAA 2002-0663, 2002.
- Cattafesta, L. N., III, Garg, S., Choudhari, M., and Li, F., "Active Control of Flow-Induced Cavity Resonance," AIAA 97-1804, 1997.
- Cattafesta, L.N., et.al., "Prediction and Active Control of Flow-Induced Weapons Bay Acoustics," Final Report, High Technology Corporation, 1999.
- Cattafesta, L. N. III, Shukla, D., Garg, S., and Ross, J. A., "Development of an Adaptive Weapons-Bay Suppression System," AIAA 99-1901, 1999.
- Cattafesta, L., Song, Q., Williams, D., Rowley, C. and Alvi, F., "Active Control of flow-induced cavity oscillations," *Progress in Aerospace Sciences*, Vol. 44, pp. 479-502, 2008.
- Chokani, N., and Kim, I., "Suppression of Pressure Oscillations in an Open Cavity by Passive Pneumatic Control," AIAA 91-1729, 1991.
- Clarke, D. W., Mhtadi, C., and Tuffs, P. S., Generalized Predictive Control – Part I. The Basic Algorithm, *Automatica*, Vol. 23, No. 2, pp. 137-148, 1987.
- Clarke, D. W., Mhtadi, C., and Tuffs, P. S., Generalized Predictive Control – Part II. Extensions and Interpretations, *Automatica*, Vol. 23, No. 2, pp. 149-160, 1987.
- Dudley, J., "Leading Edge Passive Devices for Control of Supersonic Cavities" Ph.D. Dissertation, Mechanical and Aerospace Engineering, University of Florida, 2010.
- Dudley, J., Shumway, G., Tinney, C. and Ukeiley, L., "Flow Characteristics of the University of Florida-REEF Supersonic Wind Tunnel," AIAA Paper 2008-3942. 38th AIAA Fluid Dynamics Conference, 2008.
- Grant, I., & Owens, E. H., Confidence interval estimates in PIV measurements of turbulent flows. *Applied Optics*, 29(10), 1400-1402, 1990.
- Griffin, J., Schultz, T., Holman, R., Ukeiley, L. S., & Cattafesta, L. N., Application of multivariate outlier detection to fluid velocity measurements. *Experiments in Fluids*, 49(1), 305-317, 2010.
- Heller, H., and Bliss, D., "The Physical Mechanism of Flow-Induced Pressure Fluctuations in Cavities and Concepts for Their Suppression," AIAA Paper 75-491, 1975.
- Heller, H., and Delfs, J., "Cavity Pressure Oscillations: The Generating Mechanisms Visualized," *Journal of Sound and Vibration*, Vol. 196, No. 2, pp. 248–252, 1996.
- Hubert, M., & Van der Veeken, S. Outlier detection for skewed data. *Journal of Chemometrics*, 22(3-4), 235-246, 2008.

- Kegerise, M.A., Cabell, R.H., and Cattafesta, L., "Real-time feedback control of flow-induced cavity tones — Part 1: Fixed-gain control," *Journal of Sound and Vibration*, Vol. 307, Issues 3-5, pp. 906-923, 2007.
- Kegerise, M.A., Cabell, R.H., and Cattafesta, L., "Real-time feedback control of flow-induced cavity tones — Part 2: Adaptive control," *Journal of Sound and Vibration*, Vol. 307, Issues 3-5, pp. 924-940, 2007.
- Kook, H., Mongeau, L., Brown, D. V., and Zorea, S., Analysis of the Interior Pressure Oscillations Induced by Flow Over Vehicle Openings, *Noise Control Engineering Journal*, Vol. 45, No. 6, pp. 223-234, (1997).
- Krishnamurty, K., "Acoustic Radiation from Two Dimensional Rectangular Cutouts in Aerodynamic Surfaces," NACA Technical Note 3487, Aug. 1955.
- Lamp, A. M., and Chokani, N., "Computation of Cavity Flows with Suppression Using Jet Blowing," *Journal of Aircraft*, Vol. 34, No. 4, pp. 545-551, July-Aug. 1997.
- Lawson, S., and Barakos, G., "Review of Numerical Simulations for High-Speed, Turbulent Cavity Flows," 47, pp. 186-216, 2011.
- McGrath, S. F., and Shaw, L. L., Jr., "Active Control of Shallow Cavity Acoustic Resonance," AIAA 96-1949, June 1996.
- Maury, R., Koenig, M., Cattafesta, L., Jordan, P., Delville, J., Bonnet, J.-P., and Gervais, Y., Extremum-Seeking Optimization of Fluidic Jet-Noise Control, 15th AIAA/CEAS Aeroacoustics Conference (2009-5), AIAA Paper 2009-3132.
- Murray, N., Sallstrom, E., & Ukeiley, L., Properties of subsonic open cavity flow fields, *Physics of Fluids*, 21, 16, 2009.
- Nelder, J. A., and Mead, R., A Simplex Method for Function Minimization, *Computer Journal*, Vol. 7, No. 4, pp. 308-313, 1965.
- Press, W. H., Flannery, B. P., Teukolsky, S. A., and Vetterling, W. T., Numerical Recipes in Fortran, 2nd edition, Cambridge University Press, 1992.
- Rockwell, D., and Naudascher, E., "Review: Self-sustaining Oscillations of Flow Past Cavities," *Trans. A.S.M.E., J. Fluids Eng.*, 100:152-165, 1978.
- Roshko, A., "Some Measurements of Flow in a Rectangular Cutout, NACA Technical Note 3488, Aug. 1955.
- Rossiter, J. E., "Wind-Tunnel Experiments on the Flow over Rectangular Cavities at Subsonic and Transonic Speeds," Aeronautical Research Council Reports and Memoranda, No. 3438, Oct. 1964.
- Rowley, C. W., Williams, D. R., Colonius, T., Murray, R. M., and Macmynowski, D. G., "Linear Models for Control of Cavity Flow Oscillations," *J. Fluid Mech.*, Vol. 547, pp. 317-330, 2006.
- Rowley, C. and Williams, D., "Dynamics and Control of High-Reynolds-Number Flow over Open Cavities," *Annual Review of Fluid Mechanics*, Vol. 38, pp. 251-276, 2006.
- Shaw, L. L., "Suppression of Aerodynamically Induced Cavity Oscillations," AFFDL-TR-79-3119, 1979.
- Shaw, L., "Active Control for Cavity Acoustics," AIAA 98-2347, 1998.
- Stanek, M., Raman, G., Kibens, V., Ross, J., Odedra, J., and Peto, J., "Control of Cavity Resonance through Very High Frequency Forcing," AIAA 2000-1905, 2000.
- Takahashi, H., Liu, F., Palavicini, M., Oyarzun, M., Griffin, J., Ukeiley, L., and Cattafesta, L., Progress on Active Control of Open Cavities, 49th AIAA Aerospace Sciences Meeting, AIAA Paper 2011-1221, 2011.

- Tian, Y., Song, Q., and Cattafesta, L., Adaptive Feedback Control of Flow Separation, 3rd AIAA Flow Control Conference, AIAA Paper 2006-3016, 2006.
- Ukeiley, L. S., Ponton, M. K., Seiner, J. M., and Jansen, B., "Suppression of Pressure Loads in Cavity Flows," AIAA Journal, Vol. 42, No.1, pp. 70-79, 2004.
- Ukeiley, L. S., Sheehan, M., Coiffet, F., Alvi, F. S., Arunajatesan, S., and Jansen, B., "Control of Pressure Loads in Geometrically Complex Cavities," Journal of Aircraft, Vol. 45, No. 3, pp. 1014–1024, 2008.
- Unalms, O., Clemens, N. and Dolling, D., "Experimental study of shear layer/acoustics coupling in mach 5 cavity flow," AIAA Journal, Vol. 39(2), pp. 242–252, 2001.
- Vakili, A. D., and Gauthier, C., 1994, "Control of Cavity Flow by Upstream Mass-Injection," Journal of Aircraft, Vol. 31, No. 1, pp. 169-174, Jan. - Feb. 1994.
- Venugopal, R., and Bernstein, D. S., Adaptive Disturbance Rejection Using ARMARKOV System Representation, Proceedings of the 36th Conference on Decision & Control, pp. 1884-1889, 1997.
- Zhaung, N., Alvi, F., Alkilsar, M. and Shih, C., "Aeroacoustic properties of supersonic cavity flows and their control," AIAA Journal, Vol. 44(9), pp. 2118–2128, 2006.